A semiempirical model of the normalized radar cross-section of the sea surface
1. Background model

Vladimir Kudryavtsev

Marine Hydrophysical Institute, National Academy of Science, Sebastopol, Ukraine

Nansen International Environmental and Remote Sensing Center, St. Petersburg, Russia

Danièle Hauser and Gérard Caudal

Centre d'Etude des Environnements Terrestres et Planétaires, Centre National de la Recerche Scientifique, Université de Versailles, Vélizy, France

Bertrand Chapron

Institut Français de Recherche pour l'Exploitation de la Mer, Plouzané, France

[1] Multiscale composite models based on the Bragg theory are widely used to study the normalized radar cross-section (NRCS) over the sea surface. However, these models are not able to correctly reproduce the NRCS in all configurations and wind wave conditions. We have developed a physical model that takes into account, not only the Bragg mechanism, but also the non-Bragg scattering mechanism associated with wave breaking. A single model was built to explain on the same physical basis both the background behavior of the NRCS and the wave radar Modulation Transfer Function (MTF) at HH and VV polarization. The NRCS is assumed to be the sum of a Bragg part (two-scale model) and of a non-Bragg part. The description of the sea surface is based on the short wind wave spectrum (wavelength from few millimeters to few meters) developed by *Kudryavtsev et al.* [1999] and wave breaking statistics proposed by *Phillips* [1985]. We assume that non-Bragg scattering is supported by quasi-specular reflection from very rough wave breaking patterns and that the overall contribution is proportional to the white cap coverage of the surface. A comparison of the model NRCS with observations is presented. We show that neither pure Bragg nor composite Bragg model is able to reproduce observed feature of the sea surface NRCS in a wide range of radar frequencies, wind speeds, and incidence and azimuth angles. The introduction of the non-Bragg part in the model gives an improved agreement with observations. In Part 2, we extend the model to the wave radar MTF problem.   *INDEX TERMS:* 4275 Oceanography: General: Remote sensing and electromagnetic processes (0689); 4560 Oceanography: Physical: Surface waves and tides (1255); 4504 Oceanography: Physical: Air/sea interactions (0312); 4506 Oceanography: Physical: Capillary waves; *KEYWORDS:* ocean surface waves, radar cross-section, short wind waves, wave breaking, Bragg scattering, non-Bragg scattering

1. Introduction

[2] Models of the normalized radar cross-section (NRCS) of the sea-surface at intermediate incidence angles are usually treated as a composite models describing the combined effects of Bragg scattering mechanism (effective for surface ocean waves whose wavelengths are of the order of the electromagnetic wave) and local-titling effects due to longer underlying waves [*Plant*, 1986; *Donelan and Pierson*, 1987; *Romeiser et al.*, 1994; *Romeiser and Alpers*, 1997;

Janssen et al., 1998]. However, it is recognized that using this kind of models, it is difficult to obtain a consistent description of the normalized radar cross-section over a large range of radar frequencies, incidence angles, for the different polarization states and various conditions of wind and waves. In particular, it has been mentioned in several publications, that models which may provide consistent results for VV polarization, are not in agreement with observations for HH polarization [e.g., *Plant*, 1990; *Janssen et al.*, 1998]. These models do not correctly reproduce the observed azimuthal behavior of the NRCS at both HH and VV polarizations [*Quilfen et al.*, 1999], and fail to explain observed NRCS

modulations by long surface wave [e.g., *Schmidt et al.*, 1995]. Explanations proposed to interpret this shortcoming, are usually based on the idea that non-Bragg scattering plays a significant role (which is more important in HH than in VV polarization). The experimental evidence of this fact is a large deviation of measured polarized ratios from Bragg-predicted values [*Thompson et al.*, 1998; *Horstmann et al.*, 2000].

[3] In this context, the general goal of this set of two papers (Part I and Part II) is to present a semiempirical model of the NRCS that takes into account radio wave scattering from breaking waves. As intended, the model should describe both the background radar features of the sea surface and modulations of the NRCS by long surface waves (radar Modulation Transfer Function [MTF]) at VV and HH polarization, in a large range of radio wave frequencies, incidence angles, and wind conditions. It will be shown that model developed can explain both the observed dependence of the background NRCS with incidence angle, radar frequency, wind speed and polarization state (part I), and measurements of wave radar MTF (part II).

[4] We consider VV and HH radar backscattering at moderate incidence angles (specular reflection is neglected). Bragg and non-Bragg scattering mechanisms are conceptually distinguished. In section 2, we present the governing equations for the model. The Bragg part follows the standard approach of the composite Bragg theory [*Bass et al.*, 1968; *Wright*, 1968; *Plant*, 1990] which takes into account the Bragg scattering due the surface waves with wavelengths of the order of the electromagnetic wavelength, superposed on longer tilting waves. For the non-Bragg part, we extend the proposed phenomenological approach developed by *Phillips* [1988], where the overall contribution of breaking waves to the return power is related to the wave breaking fronts statistics.

[5] Section 3 describes the model of the sea surface (both wave spectrum and statistical properties of breaking waves). The model for short wind waves (wavelength from a few millimeters to a few meters) follows earlier developments by *Kudryavtsev et al.* [1999], and is based on the energy balance between wind input and viscous and wave breaking dissipation. In the capillary range, the generation mechanism of parasitic capillaries is taken into account. The model contains two tuning parameters that are a saturation level and the wind exponent in the equilibrium range of the surface gravity waves. The former parameter is specified in order to fit the model mean square slope to the observations of *Cox and Munk* [1954]. The model wind exponent in the gravity range is chosen to be consistent with existing radar observations. The angular spreading of the spectral energy does not possess any tuning constant and we show that the wind exponent of the wave spectrum defines it.

[6] In section 4, we present the radar cross-section model, where the effect of tilting waves is accounted for in the second order [*Plant*, 1986]. With this approach, the NRCS is a sum of a pure Bragg term, a term due to the tilt of the longer waves, and a term due to the cross-correlation between tilt and hydrodynamics effects. Calculations of the sea surface NRCS based on this composite Bragg scattering model are compared with several sets of airborne radar data. We show that this composite Bragg scattering model is not able to reproduce multispectral radar observa-

tions at VV and HH polarization for various incidence angles. The main discrepancy between the Bragg model and the observations is related to the polarization ratio (ratio of NCRS in VV polarization to NCRS in HH polarization) and to the upwind/downwind ratio of the NRCS. As suggested, such differences are due to a significant contribution of the non-Bragg scattering mechanism. For the non-Bragg scattering, we complete the original approach of *Phillips* [1988]. At moderate incidence angles, radar returns from breaking waves are taken proportional to the surface area with enhanced roughness caused by wave breaking. Scattering from each individual breaking zone is azimuthally independent, but depends on incidence angle as for a quasi-specular reflection. The main tuning parameter of this non-Bragg scattering part is the NRCS associated with an enhanced roughness area caused by breaking waves. It is chosen to fit the experimental results of *Unal et al.* [1991] and *Masuko et al.* [1986].

[7] In section 5, we compare the results of the model with other empirical results in X-band [*Hauser et al.*, 1997] and C-band [*Horstmann et al.*, 2000; *Vachon and Dobson*, 2000]. We also compare a representation of the model in the form of truncated Fourier series, with the predictions of the empirical geophysical functions used for spaceborne systems in C-band (model CMOD for ERS [*Bentamy et al.*, 1994]) and Ku-band (model of NSCAT [*Wentz and Smith*, 1999]). We show that the model is able to reproduce the main behavior of the observed polarization ratio, with frequency, incidence, wind speed and azimuth angle.

[8] Section 6 gives a summary and conclusion of this Part I. In Part II, the sea-surface and the backscattering models are used to study the radar modulation transfer function, which relates the modulation of the NRCS to the long surface waves.

2. Radar Backscattering: Governing Equations

2.1. Bragg Scattering

[9] We consider the Bragg scattering mechanism within the frame of a two-scale model, with Bragg waves superposed on longer tilting waves [*Bass et al.*, 1968; *Wright*, 1968]. At moderate incidence angles (typically $20-60°$), the theory of radar backscattering is based on the mechanism of resonant microwave scattering from the random rough surface [e.g., *Plant*, 1990]. For a pure Bragg process, the normalized radar cross-section σ_{0br}^p is proportional to the surface elevation spectrum at the Bragg wave number:

$$\sigma_{0br}^p = 16\pi k_r^4 |G_p(\theta)|^2 F_r(\varphi, k_{br}) \tag{1}$$

where p denotes the HH or VV polarization state, $k_{br} = 2k_r \sin\theta$ is the wave number of surface waves scattering radio wave, k_r is the radar wave number, θ is the incidence angle, φ is the antenna azimuth, $F_r(\varphi, k)$ is the 2D-wave number variance (folded) spectrum of the sea surface displacement, and G_p is the Bragg scattering geometric coefficient.

[10] The folded spectrum $F_r(\varphi, k)$ is related to the directional wave number spectrum $F(\varphi, k)$ by:

$$F_r(\varphi, k) = 0.5(F(\varphi, k) + F(\varphi + \pi, k)) \tag{2}$$

ea surface the HH and VV scattering coefficients

$$|G_v(\theta)|^2 = \frac{\cos^4\theta\left(1+\sin^2\theta\right)^2}{(\cos\theta+0.111)^4} \qquad (3)$$

$$|G_h(\theta)|^2 = \frac{\cos^4\theta}{(0.111\cos\theta+1)^4}. \qquad (4)$$

; (3)–(4) are written here as given by *Plant* [1986]
; a simplified form of the complete equations
g the dielectric constant of the seawater to be
|ual to 81). It follows from equation (1) that for a
idence angle, the radar signal is defined by the level
/ind wave spectrum and its distribution in azimuth.
real conditions short wind waves scattering radio
e running along the longer surface waves (LW),
ure Bragg theory loses its validity. The composite
ering model developed by *Bass et al.* [1968] and
968] extends the Bragg theory to the case of the
sea. In the frame of such a model, each small area
W surface scatters radio waves according to the
:ory, where however incidence angle and rotation
:idence plane are random functions related to the
surface slope. The average NRCS is the result of
the "local" cross-sections of individual small
long the LWs. At moderate incidence angle and
l LW slopes, the NRCS of the sea surface is
:d by:

$$\sigma_{br}^p = 16\pi k_r^4 \overline{\left|G_p\left(\theta-\zeta_x,\zeta_y\right)^2\right| F_r\left(0,k_{br}'\right)} \qquad (5)$$

.) denotes an averaging over scales of the LWs, ζ_x
e the slopes of the tilting waves along and across
:nce plane, respectively (with x *axis* directed along
:nce plane). k_{br}' is the Bragg wave number, $k_{br}' =$
− ζ_x). The scattering coefficients G_p at polarization
are given respectively by:

$$G_v\left(\theta-\zeta_x,\zeta_y\right) = G_v(\theta-\zeta_x) \qquad (6)$$

$$'_h\left(\theta-\zeta_x,\zeta_y\right) = G_h(\theta-\zeta_x) + \left(\zeta_y/\sin\theta\right)^2 G_v(\theta) \qquad (7)$$

lly accepted that scales of the tilting LWs must
:veral times the Bragg wavelength. It is clear from
(5) that the contribution of the tilting LWs to the
NRCS appears in the second order of the LWs
:vertheless this contribution is not negligible and
iificantly influence the NRCS, especially at HH
on [e.g., *Plant*, 1986].

n-Bragg Scattering

: small incident angles (including normal inci-
lecular reflection from the sea surface is the main
m responsible of non-Bragg scattering. NRCS of
lar component is [*Valenzuela*, 1978]:

$$\sigma_{sp} = \frac{|R|^2\sec^4\theta}{2\overline{\zeta_\perp\zeta_i}}\exp\left(-\frac{\tan^2\theta}{2\overline{\zeta_i^2}}\right) \qquad (8)$$

is the reflection coefficient at normal incidence, $\overline{\zeta_i^2}$
ean square slope of waves supporting specular

reflection in the direction of incidence plane, $\overline{\zeta_i}$ is the
corresponding standard deviation, $\overline{\zeta_\perp}$ is the standard devia-
tion of slope of these waves in the direction perpendicular to
the incidence plane. It is usually accepted that wavelengths
of surface waves providing specular reflection are larger
than 3 to 10 times the radar wavelength. Mean squared
slope of these waves is generally small; hence the specular
reflection dominates the NRCS at small (close to normal)
incidence angle. With increasing incidence (at $\theta > 15-20°$)
their role becomes negligible in comparison with the Bragg
scattering component. In the following, we will not con-
sider this specular component since we are interested in
observations at incidence angles larger than 20°.

[13] In addition, it has been recognized that the compo-
site Bragg theory is not fully appropriate to explain and
represent the radar signature at moderate incidence angles
($\theta > 20°$). This is revealed in particular by the existence of
"sea spikes" in high-resolution radar observations or by
large deviations of the observed polarization ratio (ratio of
the radar return in VV polarization to that in HH) from
Bragg theory predictions. Results of the analysis of
NSCAT dual-polarized data set [*Quilfen et al.*, 1999; *Tran*,
1999] or of the combined analysis of ERS and RADAR-
SAT observations [*Horstmann et al.*, 2000] are examples
showing that the standard composite Bragg theory is not
appropriate at moderate incidence angles. *Plant et al.*
[1999] also showed that the polarization ratio observed
in a wave-tank is not consistent with the standard compo-
site Bragg theory.

[14] A number of plausible mechanisms have been sug-
gested to explain this. From their wave-tank measurements,
Plant et al. [1999] suggest that the presence of bound
waves travelling at the speed of the dominant wave
modifies the mean square slope and mean tilt angle, and
thus affects the upwind-to downwind ratio of NRCS, and
the polarization ratio. Introducing the statistical properties
of these bound waves in the composite Bragg theory, *Plant
et al.* [1999] were able to reproduce the observed features
of the NRCS. However, they recognize that in real con-
ditions on the ocean surface, even if bound tilted waves
have been evidenced, their spectral density is too small to
affect the radar signature.Other mechanisms, based on non-
Bragg scattering, have been invoked to explain the radar
signature: diffraction of radio waves on sharp wedges of
breaking crests [*Kalmykov and Pustovoytenko*, 1976], quasi-
specular reflection from steep forward face of breaking
waves [*Kwoh and Lake*, 1984; *Melville et al.*, 1988; *Wine-
brenner and Hasselmann*, 1988], increased backscattering
from intensive roughness generated by breaking waves
[*Kwoh and Lake*, 1984; *Banner and Fooks*, 1985; *Ericson
et al.*, 1999]. Here we will follow these suggestions and
propose a model, which accounts for composite Bragg and
non-Bragg scattering.

[15] Some analytical and numerical solutions of the
scattering problem have been proposed, in the past. Among
these studies we mention the recent investigations by
Lyzenga and Ericson [1998] of microwave diffraction on
a wedge corresponding to a steep Stokes wave. It was
shown that the backscattering power drops quickly when
the curvature radius r_c of the crest increases; at $k_r r_c > 1$, the
return signal becomes insignificant. Although at moderate
angles wedge-like diffraction could contribute significantly

to the observed radar backscatter, they concluded that this mechanism can be effective at low frequencies only (such as L-band). Indeed, the surface tension prevents very small surface curvature of the wave crests, which act as radar scatters at larger frequencies. So, wedge-like diffraction cannot significantly occur in K-, X-, and C-bands. Recent detailed laboratory study of radar backscattering from stationary breaking waves by *Ericson et al.* [1999] (performed at $\theta = 45°$), revealed that a strong increase of the radar return near the breaking crest occurs due to incoherent backscattering from small scale roughness generated by the breaking crest. Values of the NRCS of the enhanced roughness at the breaking crest were of the order of (−6 to −3 dB) with a polarization ratio close to unity. They concluded that the incoherent backscatter from surface disturbances generated by breaking waves might explain the origin of sea-spikes (high radar return) and small polarization ratios observed in real conditions at moderate incidence angles. They also showed that near the breaking crests, the NRCS is well reproduced by a Kirchhoff approximation for incoherent scattering, whereas far from the breaking crest, radar backscattering follows a Bragg model prediction.

[16] *Phillips* [1988] developed a fruitful phenomenological approach to describe the non-Bragg scattering. Taking into account that any non-Bragg scattering mechanism relates to the wave breaking events, Phillips described their overall contribution to the NRCS as the contribution of the scattered area associated with wave breaking fronts. If $\Lambda(\mathbf{k})d\mathbf{k}$ is the total length of wave breaking fronts (related to wave numbers in the range $\mathbf{k}$ to $\mathbf{k} + d\mathbf{k}$) per unit surface, then the scattered area (area of radar target) is proportional to $k^{-1} \Lambda(\mathbf{k})d\mathbf{k}$, and the total contribution from all the wavebreaking fronts to the sea surface NRCS is:

$$\sigma_{wb} = \int C(k/k_r, \theta, \varphi)k^{-1}\Lambda(\mathbf{k})d\mathbf{k} \tag{9}$$

where $C(k/k_r, \theta, \varphi)$ is an empirical function that we will define later from comparison of equation (9) with radar measurements. The recent results of *Ericson et al.* [1999] can be easily taken into account in equation (9). In this context, $C(k/k_r, \theta, \varphi)$ in equation (9) is directly related to the NRCS of disturbed areas near the breaking crests.

[17] Specular reflection and scattering from breaking waves randomly distributed on the sea surface are statistically independent of Bragg scattering occurring from the sea surface covered by "regular" wind waves. Hence the total NRCS of the sea surface σ_0^p can be represented as a sum of Bragg scattering (equation (5), σ_{br}^p), specular reflection σ_{sp} (equation (8)) and non-Bragg scattering from breaking waves σ_{wb} (equation (9)):

$$\sigma_0^p = \sigma_{br}^p + \sigma_{sp} + \sigma_{wb} \tag{10}$$

where, according to radar observations, it is suggested that σ_{sp} as well as σ_{wb} are independent of polarization.

[18] To calculate the radar cross-section according to equation (10), we need to specify the wind wave spectrum and the spectral distribution of the wave breaking fronts.

The following section describes the sea surface model that will be used in the NRCS model.

3. Statistical Properties of the Sea Surface
3.1. Governing Equations and Background Spectrum

[19] The model considered here is aimed at describing the statistical properties of the sea surface that are relevant to the radar study from L to Ka bands. The wind wave scales related to this problem range from short gravity to capillary surface waves, respectively. Description of the wave spectrum is based on the energy balance equation which is more convenient to use in terms of the wave action spectrum $N(\mathbf{k})$ [e.g., *Phillips*, 1977]:

$$\frac{\partial N(\mathbf{k})}{\partial t} + \left(c_{gi} + u_i\right)\frac{\partial N(\mathbf{k})}{\partial x_i} - k_j\frac{\partial u_j}{\partial x_i}\frac{\partial N(\mathbf{k})}{\partial k_i} = Q(\mathbf{k})/\omega \tag{11}$$

where c_{gi} and u_i are components of wave group velocity and surface current; i and j = 1, 2; ω and $\mathbf{k}$ are the frequency and wave number vector (with components k_i) related by the dispersion relation:

$$\omega^2 = gk + \gamma k^3 \tag{12}$$

$k = |\mathbf{k}|$, g is the acceleration of gravity, γ is the surface tension, $Q(\mathbf{k})$ is the source of wave energy. The elevation spectrum $F(\mathbf{k})$, energy spectrum $E(\mathbf{k})$, and wave action spectrum $N(\mathbf{k})$ are related to each other by: $E(\mathbf{k}) = (\omega^2/k)F(\mathbf{k})$, $N(\mathbf{k}) = E(\mathbf{k})/\omega = (\omega/k)F(\mathbf{k})$. Note also the definition of the saturation spectrum $B(\mathbf{k})$ (or the surface curvature spectrum) that is used throughout the paper: $B(\mathbf{k}) = k^4F(\mathbf{k})$.

[20] In the following, we use the same equation (equation (11)) for the description of both the background spectrum and its modulations by long surface waves. The background spectrum results from the solution of the equation $Q(\mathbf{k}) = 0$, and the modulation of the short wind waves by LW can be found as a solution of the linearized equation (11) for small disturbances of the spectrum (see Part 2). The form of the spectral source $Q(\mathbf{k})$ is not exactly known, so that concrete results can only be obtained by using simplifications and hypotheses concerning the role of different energy source/sink terms. The present study is based on the model of the short wind wave spectrum developed by *Kudryavtsev et al.* [1999] (hereinafter KMC99), but with some modifications for application to simulation radar observations.

[21] In KMC99 the shape of the spectrum results from the physical description of the energy source. In the equilibrium range of the spectrum (for $k \gg k_p$ where k_p is the wave number of the spectral peak) this energy source is:

$$Q(\mathbf{k}) = \omega^3 k^{-5}\left[\beta_\nu(\mathbf{k})B(\mathbf{k}) - B(\mathbf{k})\left(\frac{B(\mathbf{k})}{\alpha}\right)^n + I_{pc}(\mathbf{k})\right] \tag{13}$$

where $\beta_\nu(\mathbf{k}) = \beta(\mathbf{k}) - 4\nu k^2/\omega$ is the effective growth rate, which is the difference between the wind growth rate $\beta(\mathbf{k})$ and the rate of viscous dissipation (ν is the viscosity coefficient), second term parameterizes the nonlinear energy losses discussed below, α and n are some functions of k/k_γ, where $k_\gamma = (g/\gamma)^{1/2}$ is the wave number of the minimum phase velocity, and the source term I_{pc} is the energy input due to generation of parasitic capillaries. To further describe

the nonlinear energy losses, we distinguish two ranges of gravity waves: in the first interval ($k < k_{wb}$, with $k_{wb} \approx 2\pi/0.15$ rad/m), waves break and loose energy generating turbulence, while in the second interval ($k_{wb} < k < 1/2k_\gamma$), short gravity waves break and loose energy generating parasitic capillaries. In addition, three-wave resonant interactions redistribute energy from a vicinity of $k \sim k_\gamma$ toward shorter and longer waves.

[22] Short gravity waves generating parasitic capillaries provide a cascade energy transfer from gravity to capillary range of the spectrum described by term I_{pc}. Wave numbers of parasitic capillaries **k** and **k_g** generating gravity waves are collinear and their modulus are related as:

$$k_g = k_\gamma^2/k \qquad (14)$$

Generation of parasitic capillaries provides the energy losses $D(\mathbf{k_g})$ of short gravity waves, and as it was suggested by KMC99 the dimensionless source I_{pc} reads

$$I_{pc}(\mathbf{k}) = \hat{D}(\mathbf{k_g})\phi(k/k_\gamma) \qquad (15)$$

where $\hat{D}(\mathbf{k_g}) = \omega_g^{-3}k_g^5 D(\mathbf{k_g})$ is the dimensionless energy dissipation, $\omega_g = \omega(k_g)$, and $\phi(k/k_\gamma)$ is a filter function, which restricts the action of source $I_{pc}(\mathbf{k})$ in the k-space. Its physical meaning is that parasitic capillaries cannot be generated by all gravity waves. The crest of decimeter and longer gravity waves (waves with $k > k_{wb}$) breaks and an individual wave loses its energy generating turbulence rather than generating trains of parasitic capillaries. Thus, the filter function has to be close to 1 in the interval $2 < k/k_\gamma < k_\gamma/k_{wb}$ and to vanish outside this range. In the gravity range the energy losses are compensated by energy input from wind, hence

$$I_{pc}(\mathbf{k}) = \beta_\nu(\mathbf{k_g})B(\mathbf{k_g})\phi(k/k_\gamma) \qquad (16)$$

KMC99 obtained the shape of the spectrum in the equilibrium range (at $k \gg k_p$) by considering the solution of Equation (11) with source (13) under conditions of a steady wind and uniform surface currents. Thus equation $Q(k) = 0$ gives (see KMC for more details):

$$B_{eq}(\mathbf{k}) = \frac{\alpha}{2^{1/n}}\left[\left(\beta_\nu(\mathbf{k}) + (\beta_\nu^2(\mathbf{k}) + 4I_{pc}(\mathbf{k})/\alpha)^{1/2}\right)\right]^{1/n} \qquad (17)$$

The growth rate parameter β is traditionally parameterized as a quadratic dependence on friction velocity, u_*:

$$\beta(\mathbf{k}) = C_\beta(u_*/c)^2 \cos^2\varphi \qquad (18)$$

where C_β is a parameter, φ is an angle between wind and wave directions. The angular dependence of β in (18) is defined in accordance with model predictions [e.g., Townsend, 1972; Mastenbroek, 1996]. The physical meaning of the $\cos^2\varphi$ angular term in equation (18) is that within the frame of the sheltering mechanism of short (hence slow) wave generation (which is the most plausible mechanism, e.g., Belcher and Hunt [1993]), surface pressure acting on

the forward slope is proportional to the square of the wind velocity component perpendicular to the wave crest. In the present paper, parameter C_β is defined according to the parameterization of Stewart [1974],

$$C_\beta = 1.5(\rho_a/\rho_w)(\kappa^{-1}\ln(\pi/kz_0) - c/u_*) \qquad (19)$$

where z_0 is the roughness scale, ρ_a and ρ_w are the air and water density, and $\kappa = 0.4$ is the Von Karman constant.

[23] Parameterization of the growth rate in the form of (18) predicts that wave energy vanishes in the crosswind directions. Obviously, this fact is not compatible with radar observations, which do show a crosswind backscatter return. Random fluctuations of wind velocity and impact of dominant surface waves may explain the observed energy in crosswind directions. Another mechanism, which may contribute to the filling of the gap of spectral energy in the crosswind directions is the nonlinear four-wave resonant interaction, for which a standard approximation is described as a diffusion operator in the two-dimensional wave number space [Hasselmann and Hasselmann, 1981]. Taking into account this process is out of the scope of the present study. To account for this fact, we replace $\cos^2(\varphi)$ angular dependence in (18) by $\exp(-\varphi^2)$. This exponent form is close to $\cos^2(\varphi)$ at small and moderate azimuths but provides a wind energy input in the crosswind directions. Moreover we suggest applying such an angular behavior for the effective growth rate β_ν, i.e.:

$$\beta_\nu(\mathbf{k}) = \left(C_\beta\frac{u_*^2}{c^2} - \frac{4\nu k^2}{\omega}\right)e^{-\Delta\varphi^2} \qquad (20)$$

where $\Delta\varphi = \varphi - \varphi_w$ is the angle between the direction of the wave component and the wind velocity vector φ_w. Note that hereinafter the downwind direction corresponds to $\varphi = \varphi_w$, whereas $\varphi = \varphi_w + \pi$ corresponds to the upwind direction. The drag coefficient of the sea surface (which is needed to calculate C_β and u_* in equation (20) is expressed in terms of the roughness scale parameter z_0 which is parameterized as [e.g., Smith, 1988]:

$$z_0 = a_* u_*^2/g + a_\nu \nu_a/u_* \qquad (21)$$

where ν_a is the air viscosity, a_* and a_ν are coefficients ($a_* = 0.018$, $a_\nu = 0.1$).

[24] Parameters α and n in equation (13) are the main parameters of the model. Their spectral behavior is related to the different mechanisms of energy losses. As described in KMC99, well inside the gravity range ($k_p \ll k < k_{wb} = 2\pi/0.15$ rad/m), energy losses are dominated by wave breaking and parameters α and n have to be constants ($n = n_g$ and $\alpha = \alpha_g$). In the capillary-gravity range, ($k/k_\gamma > 1/2$), the dominant energy loss is due to 3-wave interactions, and is quadratic in the saturation energy density B(k), so that parameter n must be n = 1, and α is another constant $\alpha = \alpha_\gamma$. In the transitional interval $k_{wb} < k < 1/2k_\gamma$ the energy losses are dominated by small-scale wave breaking which is accompanied by emitting of parasitic capillaries. Since in this interval both gravity and surface tension govern wave dynamics, we suggest (using dimensional arguments) that

parameters α and n must be function of k/k_γ and patch the corresponding constants in the gravity range and at $k \approx k_\gamma$. So, we chose the n-function in the form:

$$1/n = \left(1 - 1/n_g\right)f\left(k/k_\gamma\right) + 1/n_g \qquad (22)$$

where $f(k/k_\gamma)$ has to be 0 at $k/k_{wb} < 1$ and 1 at $k/k_\gamma \propto 1$. To define function f, we fist note that wave numbers of parasitic capillaries $\mathbf{k}$ and generating gravity waves k_g are collinear and of their modulus are related by equation (14). Hence the interval of change of function $f(k/k_\gamma)$ is related to the interval of change of function $\phi(k/k_\gamma)$ introduced in equation (15). Thus the derivative of $f(k/k_\gamma)$ has to coincide with the filter function: i.e.

$$f'\left(k_\gamma/k\right) = \phi\left(k/k_\gamma\right) \qquad (23)$$

A convenient way to choose the filter function ϕ is:

$$\phi\left(\hat{k}\right) = U\left(\hat{k} - \hat{k}_l\right) - U\left(\hat{k} - \hat{k}_h\right) \qquad (24)$$

where $\hat{k} = k/k_\gamma$ is dimensionless wave number, $U(x)$ is the step-like function $U(x) = 1/2(\mathrm{erf}(2x) + 1)$, $\hat{k}_1$ and $\hat{k}_h$ are low and high frequency limits of the filter function which are: $\hat{k}_1 = 1.5$ and $\hat{k}_h = k_\gamma/k_{wb}$. Then, according to (23) f is:

$$f\left(k/k_\gamma\right) = f^{-1}(\infty)\int_0^{k/k_\gamma} \phi\left(k_\gamma/k_g\right)d\left(k_g/k_\gamma\right) \qquad (25)$$

To define the function $\alpha(k/k_\gamma)$, we use the fact that in the transitional interval $k_{wb} < k < 1/2k_\gamma$ and , at moderate to high wind speeds, viscous dissipation can be neglected, and the shape of the spectrum in the wind direction is $B = \alpha(k/k_\gamma)\left(C_\beta u_*^2/c^2\right)^{1/n(k/k_\gamma)}$. A dimensional analysis shows the saturation spectrum to be a function of u_*/c and k/k_γ only, i.e. $B = B(u_*/c, k/k_\gamma)$. In our model, we have determined the functional dependence of B on k/k_γ via the parameter $n(k/k_\gamma)$. Hence it is reasonable to assume the shape of the spectrum to be proportional to $\left(u_*/c\right)^{2/n(k/k_\gamma)}$. This implies that $\alpha(k/k_\gamma)C_\beta^{1/n(k/k_\gamma)}$ is a constant in the transitional interval. Thus the dependence of α on k/k_γ appears via $n(k/k_\gamma)$ as:

$$\log(\alpha) = \log(a) - (1/n)\log(\bar{C}_\beta) \qquad (26)$$

where a is a tuning constant, and $\bar{C}_\beta$ is the growth rate parameter averaged over the transitional interval. Thus, the shape of the directional equilibrium wave number spectrum is defined by equation (17), where the effective growth rate and functions n and α are specified by equations (18), (22), and (26), respectively. For the radar application the directional spectrum B_{eq} (equation (17)) must be transformed to the folded spectrum B_r according to equation (2).

[25] To complete the description of the wind wave field, we need for application to radar cross-section modeling, the description of the wave breaking statistics. As a measure of wave breaking, *Phillips* [1985] introduced the total length of breaking fronts $\Lambda(\mathbf{c})d\mathbf{c}$ running with velocities in the range from $\mathbf{c}$ to $\mathbf{c} + d\mathbf{c}$. This quantity directly relates to the energy losses due to wave breaking

$$dD = bg^{-1}c^5\Lambda(\mathbf{c})d\mathbf{c} \qquad (27)$$

where b is an empirical constant estimated as $b \approx 0.06$ for stationary breaker [*Duncan*, 1981] and as $b \approx (0.003$ to

0.01) for the nonstationary one [*Melville*, 1990]. In the present study the energy dissipation due to wave breaking is parameterized as a $(n + 1)$ power of the saturation spectrum (second term in (13)). This parameterization coincides with (27) if $\Lambda(\mathbf{c})$ is defined as

$$\Lambda(\mathbf{c}) = \frac{g}{c^4}\left(\frac{B(\mathbf{k})}{\alpha}\right)^{n+1} \qquad (28)$$

and $b = 2\alpha$. To define (28) we take into account that $dD = D(\mathbf{k})d\mathbf{k}$, and that velocity of breaking fronts c and the wave number of the wave carrying a breaker are linked by dispersion relation $k = g/c^2$ (with aligned directions for $\mathbf{k}$ and $\mathbf{c}$). The a posteriori estimate of α in the gravity interval is $\alpha = 5.10^{-3}$ (see section 3.2) so that $b = 10^{-2}$ which is inside the range of empirical values of b.

3.2. Tuning of the Background Spectrum and Comparison With Measurements

[26] We have to define our two tuning constants, the constant of the equilibrium gravity range n_g, and the saturation level constant a, respectively. The constant n_g determines the wind exponent $m_g(m_g = 2/n_g)$ in the equilibrium gravity range, and its value should be specified so that the model wind exponent corresponds to the observed one. However, there is a significant scatter in the empirical estimates of the wind exponent in the gravity range, varying from 0.2 ± 0.2 [*Banner et al.*, 1989] to 1 [e.g., *Toba*, 1973]. *Unal et al.* [1991] used radar data at VV polarization (for a Bragg wavelength $\lambda_{br} \approx 30$ cm) to estimate the wind exponent. They give $m_g \approx 0.5$. *Trokhimoski and Irisov* [2000], obtained the same order of magnitude by using a compilation of radar and radiometric measurements. In the present study we take $n_g = 5$ (consequently the wind exponent $m_g = 0.4$), to be consistent with the model of *Donelan and Pierson* [1987], with the field observations of *Banner et al.* [1989], and with the estimate from microwave observations by *Unal et al.* [1991] and *Trokhimoski and Irisov* [2000]. In Figure 1, the experimental estimates of the radar wind exponent deduced from various radar experiments at VV polarization [*Unal et al.*, 1991; *Jones and Schroeder*, 1978; *Masuko et al.*, 1986] and from the CMOD-IFR2 model [*Bentamy et al.*, 1994] are shown as a function of the Bragg wave number normalized by k_γ. On the same figure the solid line shows the model wind exponent (defined as $m = 2/n$) calculated through equation (22) at $n_g = 5$ and with the f-function defined by equation (25). It is observed that the model wind exponent is in agreement with the experimental estimates in the whole range of k/k_γ.

[27] The last tuning constant a is defined in order to fit the mean square slope to the results of *Cox and Munk* [1954] inferred from optical glitter measurements. The empirical wind dependence of the mean square slope s^2 obtained by *Cox and Munk* [1954] is shown in Figure 2 (left panel) along with the model calculations

$$s^2 = \int k^{-2}B_{eq}(\mathbf{k})d\mathbf{k} \qquad (29)$$

obtained with spectrum (17) at constant $a = 2.5.10^{-3}$. The model values of the mean square slope are in reasonably good agreement with the observations. The right-hand panel of the figure presents the ratio of crosswind to upwind components
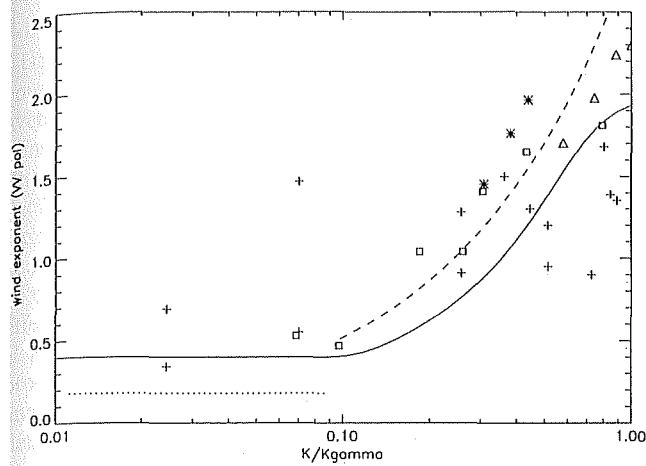
Figure 1. Radar wind exponent m as a function of the Bragg wave number normalized by k_γ. Symbols are measurements: squares for *Unal et al.* [1991], plus signs for *Jones and Schroeder* [1978], triangles for *Masuko et al.* [1986], stars for the CMOD-IFR2 empirical model [*Bentamy et al.*, 1994]. The solid line is the wind exponent of the spectrum $m = 2/n$ where n is defined by equations (22) and (25) with $n_g = 5$. The dotted line corresponds to the stereophotogrammetric observations by *Banner et al.* [1989] (m = 018, over the wavelength range $0.3 \le \lambda \le 1.6$ m).

of the mean square slope. This characteristic of the sea surface is an integral measure of the angular distribution of the short wave energy. Note that the model does not contain any special tuning parameter defining the angular distribution of waves. In the model the angular dependence appears via the angular behavior of the growth rate parameter and the n-function (defining the wind exponent). Agreement of the model with the observed estimates of the ratio of crosswind to upwind mean square slope components is a remarkable feature of the model.

[28] Figure 3 shows the model omnidirectional saturation spectra and laboratory data obtained by *Jähne and Riemer* [1990] and *Hara et al.* [1997] at wave numbers $k = 785$ rad/m,

393 rad/m, 203 rad/m, and 100 rad/m. The model calculations are also in overall agreement with the measurements done in both the capillary and the gravity ranges. This fact is important because the model only uses one constant a to determine the spectral level in the whole wave number range. The same constant provides a correct spectral level in the range of very short waves. Note also, that the model wind exponent is consistent with measurements which vary from $m = 1$ at $k = 100$ to $m = 2$ in the vicinity of the minimum phase velocity and to $m \approx 2.5$ to 3 in the capillary range.

[29] Figure 4 shows the model downwind and omnidirectional saturation spectra of short wind waves for various wind speeds (U_{10} = 3, 5, 7, 10 and 15 m/s). At low wind speed, there is a spectral gap in the vicinity of $k \approx k_\gamma$, which fills up with increasing wind. This spectral gap is caused by molecular viscosity and nonlinear redistribution of energy. At wave number $k \approx 2k_\gamma$ the cascade energy flux from short gravity waves overcomes these processes, so that the local spectral maximum does appear. Well inside the capillary range, the saturation spectrum rapidly drops. All these described features of the SW spectra are in agreement with laboratory measurements by *Jähne and Riemer* [1990] and *Zhang* [1995].

[30] For some calculations related to contributions of tilt and hydrodynamic effects, we also need to define the spectrum of long energy containing waves $B_{lw}(\mathbf{k}, c_p/U_{10})$, where c_p/U_{10} is the wave age. For this purpose we chose the empirical spectrum proposed by *Donelan et al.* [1985] with the high frequency "cut-off" correction proposed by *Elfouhaily et al.* [1997] to suppress energy at wave number exceeding $10k_p$. Then the model of the wave spectrum in the full wave number domain is presented as a sum of short waves B_{eq} and long waves spectra B_{lw}, i.e.

$$B(\mathbf{k}) = B_{lw}(\mathbf{k}, c_p/U_{10}) + B_{eq}(\mathbf{k}) \qquad (30)$$

4. Simplified NRCS Model

[31] In this section we consider the radar backscattering properties of the sea surface, using the short wind wave spectrum proposed in the previous section.
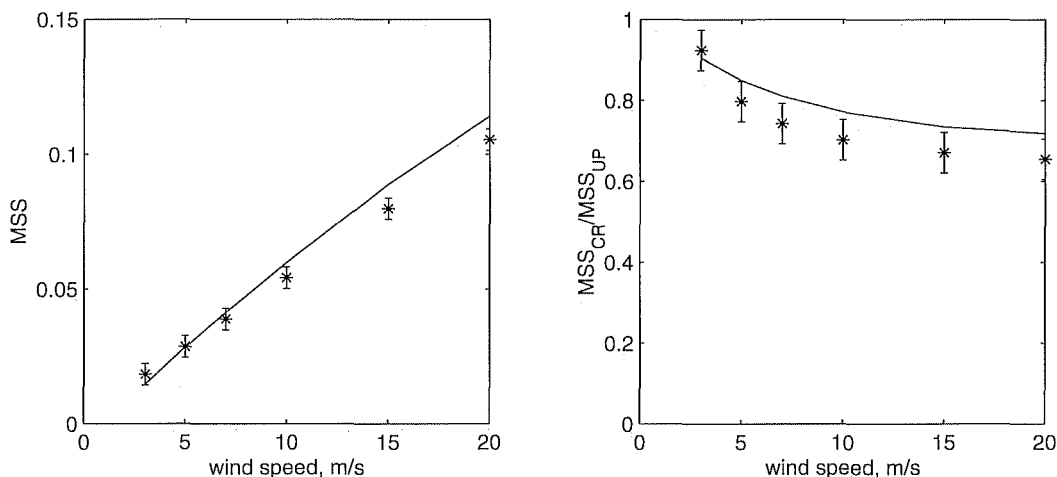
Figure 2. Mean square slope (left panel), and ratio of crosswind to upwind mean square slopes (right panel) versus wind speed. Solid lines are model predictions. Symbols are observations by *Cox and Munk* [1954].
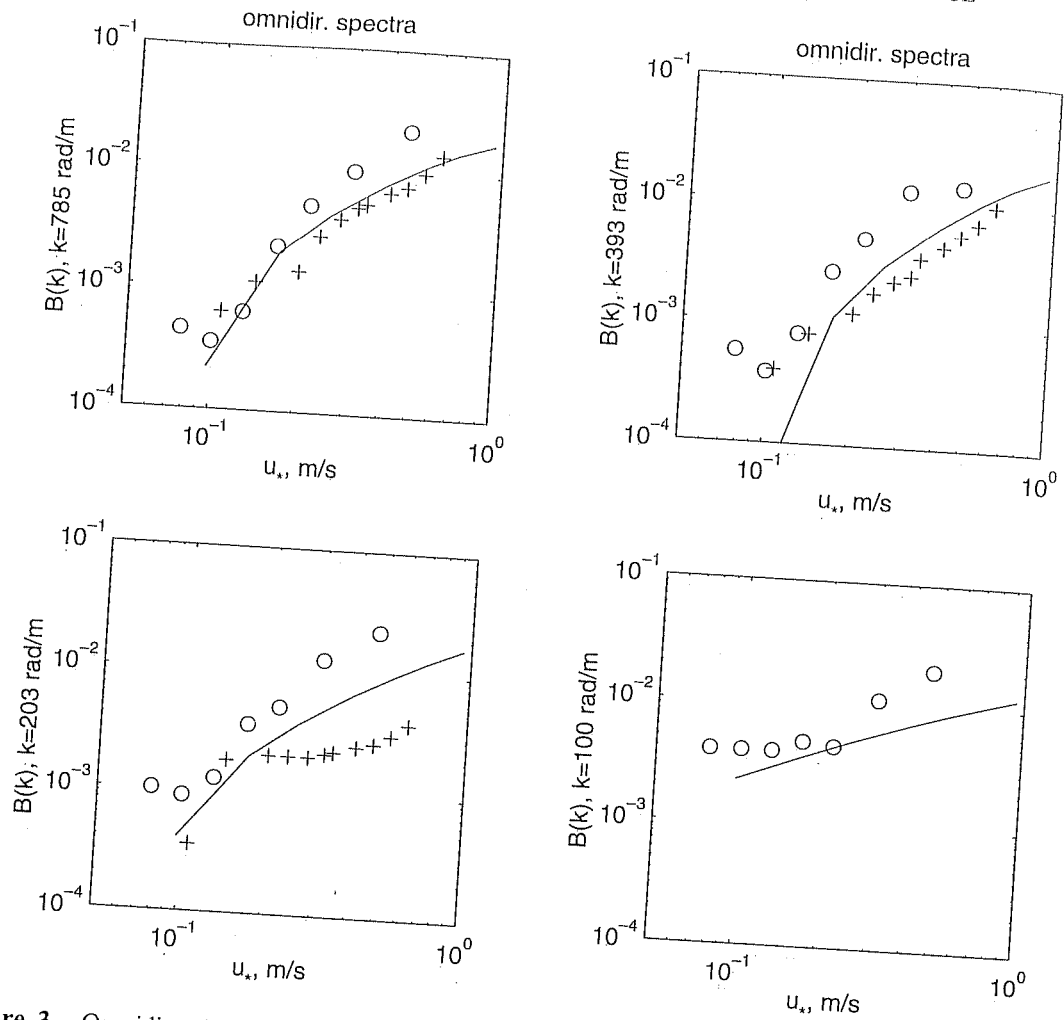
Figure 3. Omnidirectional curvature spectrum at different wave numbers as a function of friction velocity. Open circles are measurements by *Jähne and Riemer* [1990]; crosses are measurements by *Hara et al.* [1997]; solid lines are model calculations.
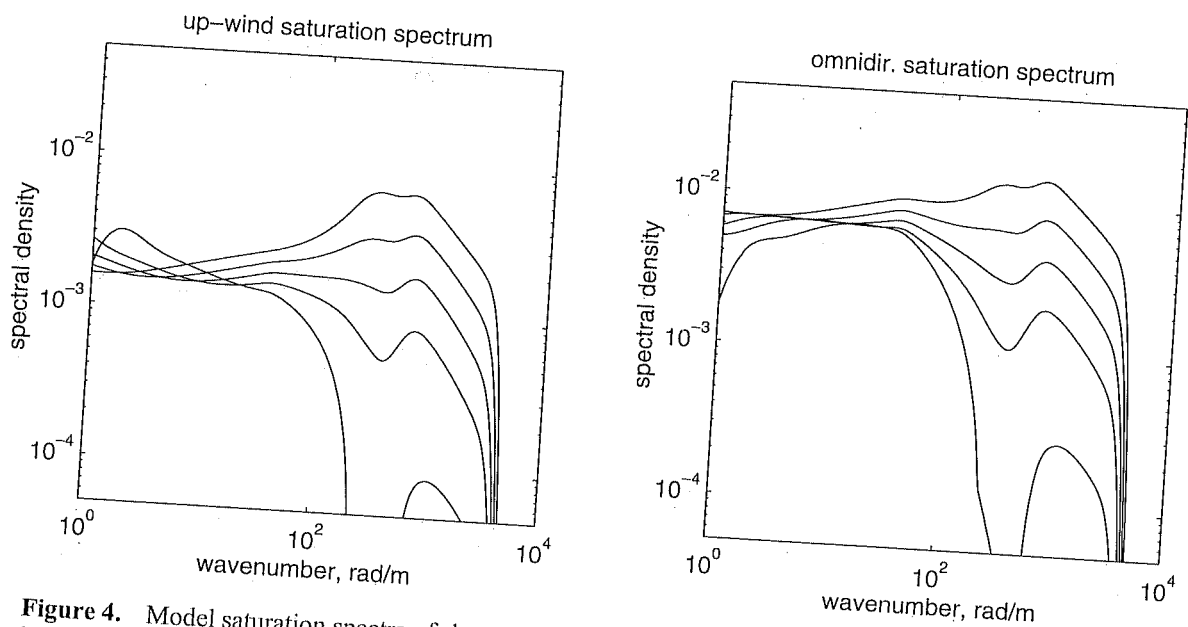

Figure 4. Model saturation spectra of short wind waves at various wind speeds (3, 5, 7, 10, 15 m/s from lower to upper curves). Downwind saturation spectra $B(0°, k)$ are in the left panel, and omnidirectional spectra $B(k)$ are in the right one.

4.1. Bragg Scattering

[32] Radar Bragg-scattering within the frame of the composite model is given by equation (5). It describes the averaged NRCS resulting from summing local cross-sections distributed along the longer (or tilting) surface waves. Their wave numbers have to be significantly smaller than the Bragg-resonant wave number k_{br}. The upper limit k_t of the range of tilting waves is defined as $k_t = t k_{br}$, where t is a constant which is usually accepted as $t = 0.1 \div 0.2$.

[33] At moderate incidence angles (when the sheltering effect is negligible), and for small mean square sea surface slopes, equation (5) can be significantly simplified. This problem has been analyzed in detail by *Plant* [1986]. Our analysis mainly follows Plant's work, except for some details and for the shape of the spectrum. If we expand equation (5) in tilting wave slope powers to second order, the spatially averaged sea surface NRCS becomes (see Appendix A for the details):

$$\sigma^p_{br}(\theta_0, \varphi) = \sigma^p_{0br}(\theta, \varphi)\left(1 + g^p\overline{\zeta_i^2} - \frac{M^p_{t0}}{B_{r0}}\overline{\zeta_i \tilde{B}_r}\right) \qquad (31)$$

where index i relates to the mean square slope of tilting waves in the direction φ of the incidence plane, $\sigma^p_{0br}(\theta)$ is the NRCS defined by equation (1), $M^p_{t0} = (1/\sigma^p_{0br})\partial\sigma^p_{0br}/\partial\theta$ is the so-called tilt component of the radar MTF, $\tilde{B}_r$ denotes the variation of the spectrum of short wind waves (scattering radio waves) due to their interaction with longer tilting waves, and g^p are the polarization coefficients defined as:

$$g^v = \frac{1}{2\sigma^{vv}_{0br}}\frac{\partial^2\sigma^{vv}_{0br}}{\partial\theta^2} \qquad (32)$$

$$g^h = \frac{1}{2\sigma^{hh}_{0br}}\frac{\partial^2\sigma^{hh}_{0br}}{\partial\theta^2} + \frac{2}{\sin^2\theta_0}\frac{|G_v|}{|G_h|}\frac{\overline{\zeta_\perp^2}}{\overline{\zeta_i^2}} \qquad (33)$$

Slopes $\overline{\zeta_i^2}$ and $\overline{\zeta_\perp^2}$ are related to the upwind and crosswind mean square slopes of tilting waves $\overline{\zeta_u^2}$ and $\overline{\zeta_c^2}$ respectively by:

$$\overline{\zeta_i^2} = \overline{\zeta_u^2}\cos^2(\varphi - \varphi_w) + \overline{\zeta_c^2}\sin^2(\varphi - \varphi_w) \qquad (34)$$

$$\overline{\zeta_i^2} = \overline{\zeta_u^2}\sin^2(\varphi - \varphi_w) + \overline{\zeta_c^2}\cos^2(\varphi - \varphi_w) \qquad (35)$$

with

$$\overline{\zeta_u^2} = \int d\varphi\cos^2\varphi\int_{k<k_t} d\ln k B(k, \varphi) \qquad (36)$$

$$\overline{\zeta_c^2} = \int d\varphi\sin^2\varphi\int_{k<k_t} d\ln k B(k, \varphi) \qquad (37)$$

where the integration is over all the tilting waves.

[34] The second term in the r.h.s. of equation (31) describes the contribution of the "pure" tilt effect, while the third term gives the impact of the cross-correlation between tilt and hydrodynamic modulations. *Plant* [1986] showed that the relative impact on the NRCS of the latter term is small in comparison with the "pure" tilt effect. It must be noted however, that within the frame of the composite Bragg model, this cross-correlation term is the only one responsible for the upwind-downwind difference in NRCS. We will assess this in the following. We can distinguish two contributions to the tilt-hydrodynamic

cross-correlation term. The first one results from modulations of Bragg scattering waves by tilting waves, and the second one results from specific features of the parasitic capillaries. As it was mentioned, parasitic capillaries being generated by short gravity waves, are spread on their forward slope, hence the coupled system "short gravity wave–parasitic capillaries" contributes to the correlation $\overline{\zeta_i\tilde{B}_r}$. This effect has never been included before.

[35] First of all let us consider the case of Bragg waves belonging to the gravity and capillary-gravity ranges of the spectrum (where the mechanism of generation of parasitic capillaries does not exist). To estimate the cross-correlation term in equation (31) we need an expression for the hydrodynamic modulation transfer function (MTF), relating the complex amplitude of spectral modulations $\hat{B}$ to the steepness of modulating longer wave KA. Interaction of short waves with the LW orbital velocity and the impact of the varying wind surface stress are two mechanisms responsible of the modulations of short wind waves. *Kudryavtsev et al.* [1997] have shown that when the impact of modulation by surface stress becomes important, it results in the enhancement of short waves on the LW crests. So, in the context of the present study this effect is not relevant, because it does not contribute to the cross-correlation term in equation (31). Thus in the MTF we have to take into account only the term describing the interaction of short waves with the LW orbital velocity. The truncated relation for the MTF simply reads [e.g., *Kudryavtsev et al.*, 1997]:

$$M(k, \varphi) = -\left(\frac{1 - i\tau}{1 + \tau^2}\right)\frac{k_1}{N(k, \varphi)}\frac{\partial N(k, \varphi)}{\partial k_1} \qquad (38)$$

where $M = \hat{B}/(\overline{B}KA)$ is the MTF for the spectral modulations, $\overline{B}$ is the spectrum averaged over the LW profile; $\tau^{-1} = T\Omega$ is the dimensionless relaxation parameter, Ω is the LW frequency, T is the relaxation time related to the energy source Q by $1/T = \partial Q/\partial E$. The straining factor in equation (38) can be written as:

$$\frac{k_1}{N(k, \varphi)}\frac{\partial N(k, \varphi)}{\partial k_1} = \cos^2\varphi\frac{\partial\ln N}{\partial\ln k} - \sin\varphi\cos\varphi\frac{\partial\ln N}{\partial\varphi} \qquad (39)$$

Kudryavtsev [1994] mentioned that the relaxation time cannot be chosen arbitrarily but that it must be directly related to the wind exponent m of the spectrum by:

$$T\omega = m/2\beta \qquad (40)$$

It is easy to check that the relaxation time with the energy source from equation (13), gives the same relation (40) if m is replaced by $2/n$.

[36] To estimate the cross-correlation term we need the imaginary part of equation (38), which is:

$$M_i = \cos^2\varphi\frac{\tau}{1 + \tau^2}m_N \qquad (41)$$

where $m_N = \partial\ln N/\partial\ln k$ is the wave number exponent of the spectrum. To obtain equation (41), we only take into account the dominant term of equation (39). Omitting the

angular term (second term in equation (39)) gives an error of the order of $(\partial \ln N / \partial \ln k)^{-1} \approx 1/4$. Then, the correlation $\overline{\zeta_i \tilde{B}_r}$ reads:

$$\overline{\zeta_i \tilde{B}_r} = B_{r0}(k, 0) \int_{k < k_t} \int_\varphi M_i \cos \varphi k^2 F(k, \varphi) k dk d\varphi$$
$$= B_{r0}(k, 0) \int_{k < k_t} m_N \int_\varphi \tau (1 + \tau^2)^{-1} \cos^3 \varphi B d\varphi d \ln k \quad (42)$$

where F and B are the elevation and saturation directional spectra of tilting waves. The cross-correlation of the LW's tilt and hydrodynamic modulations of the short waves in equation (31) becomes:

$$-\frac{M_{i0}^p}{B_{r0}} \overline{\zeta_i \tilde{B}_r} \approx g_{th} \overline{\zeta_t^2} \quad (43)$$

where $\overline{\zeta_t^2} = \int \int_{k < k_t} B d \ln k d\varphi$ is the mss of tilting waves, and coefficient g_{th} is:

$$g_{th} = -M_{i0}^p \frac{\int_{k < k_t} m_N \int_\varphi \tau (1 + \tau^2)^{-1} \cos^3 \varphi B d\varphi d \ln k}{\int_{k < k_t} \int_\varphi B d \ln k d\varphi} \quad (44)$$

To estimate the influence of the tilt-hydrodynamic term on NRCS, we use the fact that the angular distribution of wave energy in the range of tilting waves is significantly broader than angular changes in $\cos^3 \varphi$. It can be checked that equations (43)–(44) give a negative contribution of the cross-correlation term to the NRCS in the downwind radar looking direction and a positive one in the upwind direction. This term is thus responsible for one of the important characteristics of the sea surface NRCS, its upwind/downwind asymmetry.

[37] Let us now consider the case for which Bragg scattering waves belong to the capillary range. The generation mechanism of parasitic capillaries significantly affects the wave dynamics in this range. Parasitic capillaries are spread on the forward face of the generating short gravity waves. Hence, they directly contribute to the tilt-hydrodynamic cross-correlation term $\overline{\zeta_i \tilde{B}_r}$. An additional contribution can result from the modulation of the coupled system "parasitic capillaries–carrying gravity waves" by longer waves. However, one may anticipate that this impact is much weaker than the direct contribution of parasitic capillaries to $\overline{\zeta_i \tilde{B}_r}$. Note that all the capillary waves are not necessarily parasitic ones. Part of them are "regular" wind generated capillary waves, and their contribution to $\overline{\zeta_i \tilde{B}_r}$ appears through the "regular" modulations by tilting waves described by equations (43)–(44). The fraction of wave energy f_{pc} that is contained in the parasitic capillaries can be estimated by:

$$f_{pc}(\mathbf{k}) = \frac{I_{pc}(\mathbf{k})}{\beta_v(\mathbf{k}) B(\mathbf{k}) + I_{pc}(\mathbf{k})} \quad (45)$$

This is the ratio of the source of parasitic capillaries $I_{pc}(\mathbf{k})$ to the total energy source (see equations (13)–(20)). Trains of parasitic capillaries are spread on the forward slope of generating gravity waves. Hence, if we introduce an averaged tilt of the parasitic capillary trains $\bar{\theta}_{pc}$, the contribution of parasitic capillaries to $\overline{\zeta_i \tilde{B}_r}$ is:

$$\overline{\zeta_i \tilde{B}_r} = -\bar{\theta}_{pc} f_{pc} \Delta B(k_{br}, \varphi)$$

and their contribution to the tilt-hydrodynamic part of the NRCS is

$$-\frac{M_{i0}^p}{B_{r0}} \overline{\zeta_i \tilde{B}_r} = g_{pc} \Delta B / B_{r0} \quad (46)$$

where

$$\Delta B(k_{br}, \varphi) = (B(k_{br}, \varphi) - B(k_{br}, \varphi + \pi)) \quad (47)$$

and coefficient g_{pc} is:

$$g_{pc} = \bar{\theta}_{pc} M_{i0}^p \quad (48)$$

Since M_{i0}^p is negative, parasitic capillaries give a positive contribution to the NRCS in the upwind direction.

[38] Finally, the relation for the NRCS within the frame of the composite Bragg scattering model can be written:

$$\sigma_{br}^p(\theta_0, \varphi) = \sigma_{0br}^p(\theta_0, \varphi)$$
$$\cdot \left(1 + g^p \overline{\zeta_i^2} + g_{th} \overline{\zeta_t^2} (1 - f_{pc}) + g_{pc} f_{pc} \Delta B / B_{r0} \right) \quad (49)$$

where coefficients g^p, g_{th}, and g_{pc} are defined by equations (32), (33), (44), (48), $\overline{\zeta_i^2}$ and $\overline{\zeta_t^2}$ are the mean square slopes along the incidence plane and the total mean square slope of the tilting waves respectively, ΔB is defined by equation (47).

[39] The coefficients g^p calculated from expressions (32)–(33) are shown in Figure 5 as a function of incidence angle. As one might expect, the influence of the mean square slope of long tilting waves on the NRCS is higher in HH polarization than in VV. For large incidence angles the role of tilting waves increases very rapidly in HH polarization, whereas it decreases in VV. The solid line in the right panel shows the total polarization coefficient g^h. The dashed line is related to the "truncated" coefficient where the cross-polarization term (second term in equation (33)) is not taken into account. This figure indicates that the contribution to g^h of the cross-polarization term remains small.

[40] The relative impact of the pure tilt term (second term in equation (49)) and of the cross-correlation effect (third and fourth terms in equation (49)) are shown in Figure 6 as a function of incidence angle, for C- and Ku-bands in the upwind direction for a wind speed of 10 m/s. The impact of tilting waves (via pure tilt and cross tilt-hydrodynamics correlation) is not very sensitive to the radar frequency, although it is slightly stronger at the highest frequency (Ku-band). For both frequencies, the contribution of the pure tilt effect is larger than the cross-correlation effect. This result confirms the conclusion obtained by *Plant* [1986]. However, the cross-correlation term has an important physical significance, since in the context of a composite Bragg theory, it is the only term providing the upwind-downwind NRCS difference. Whether this term can reproduce the observed upwind-downwind asymmetry of the NRCS, will be discussed later. It is also worthwhile to note the rapid increase of the tilt-hydrodynamic contribution at Ku-band for large incidence angles (at HH polarization it is more apparent). This effect is related to the dominant role of parasitic capillaries in the Bragg scattering at large incidence and high frequency. Note also that the relative impact of the pure tilt effect at HH polarization is close to 1. At first this demonstrates its importance, but somehow shows that a decomposition of the "exact" solution in series on $\overline{\zeta_t^2}$-powers (strictly say) loses
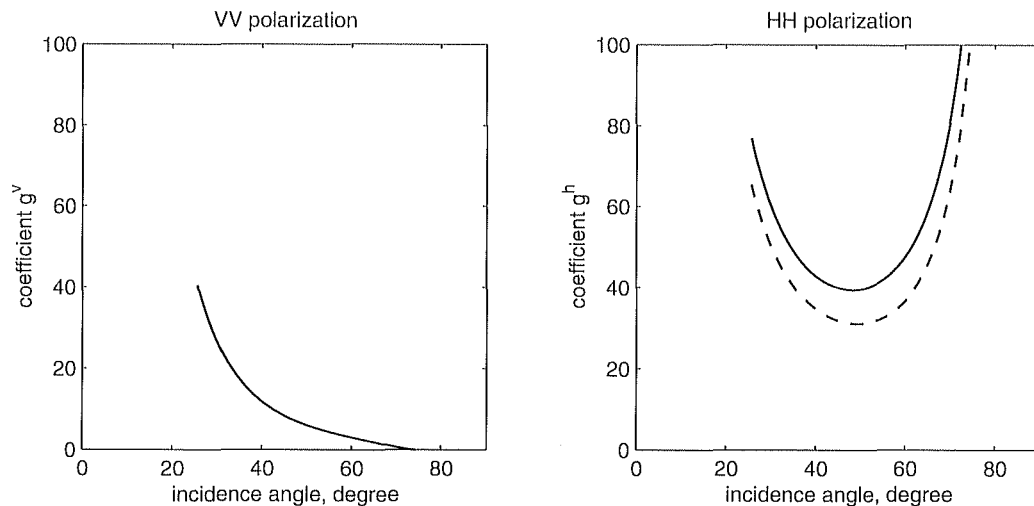
Figure 5. Coefficient g^v (left panel) and g^h (right panel) defined by equations (32)–(33) as a function of incidence angle. In the right panel (HH polarization), the solid line is the total coefficient g^h, and the dashed line is g^h without accounting for the cross-polarization effect (first term in equation (33) only).

its validity. Nevertheless, we assume we can tolerate this mathematical inaccuracy.

[41] To summarize, Bragg scattering is described by the composite model (equation (49)) with (equation (1)). It is completely defined by the spectrum of wind waves and mainly by its high frequency range. The short wind wave spectrum is given by equation (17). The parameter α of this spectrum was tuned so that the model slope variance coincides with the field observations of *Cox and Munk* [1954]. The angular spreading has no tuning constant and the azimuth dependence of σ_{br}^p is not adjusted. Within the frame of the present model, the angular spreading of the spectrum is related to the wind exponent $m = 2/n$. In the composite Bragg scattering model, one needs to specify also the range of the tilting waves. This appears in the model via the tilting wave

slope variance. In the present study we choose $t = 0.2$ ($k_t = tk_{br}$) to define the upper limit of tilting waves.

4.2. Results of the Bragg Model Compared With Observations

[42] Before we present the model for the non-Bragg scattering, we discuss here some comparisons for the polarization ratio P ($P = \sigma_0^{vv}/\sigma_0^{hh}$) between observations and the present Bragg model. This is to illustrate the limits of the Bragg model. We consider separately the results from the pure Bragg part (equations (1), (3), and (4)) and the composite Bragg model (equation (49)).

[43] Figure 7 shows the azimuthal behavior of the polarization ratio P at X-band, incidence 40°, and for a wind speed of 10 m/s. The observations were collected during the
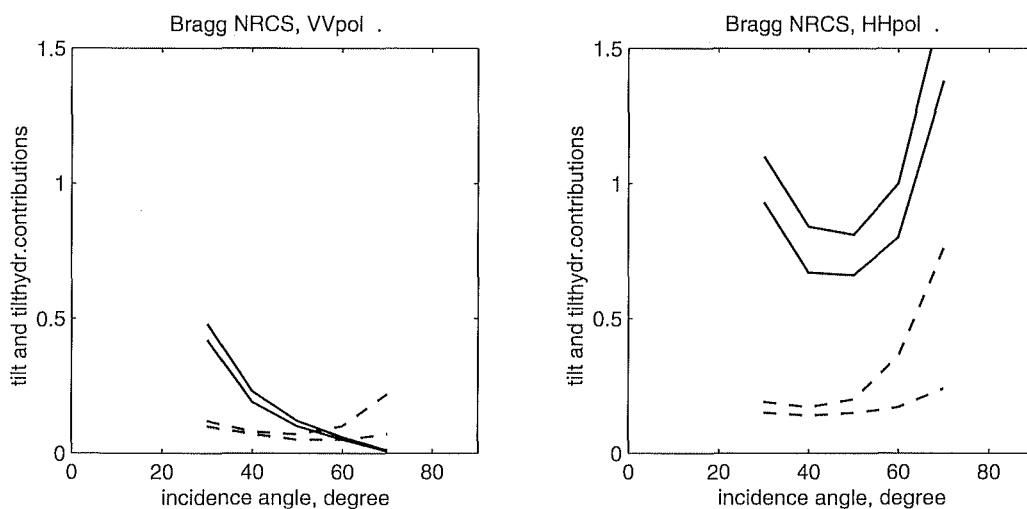
Figure 6. Relative contribution of the pure tilt effect (the second term in the brackets in equation (49); solid lines in the plots) and cross tilt-hydrodynamic effect (the third term in the brackets in equation (49); dashed lines in the plots) to the Bragg scattering. The left panel is for VV polarization, and the right one is for HH polarization. Upper lines of the same style are for Ku-band, lower lines are for C-band. Conditions: wind speed is 10 m/s, upwind radar look direction.
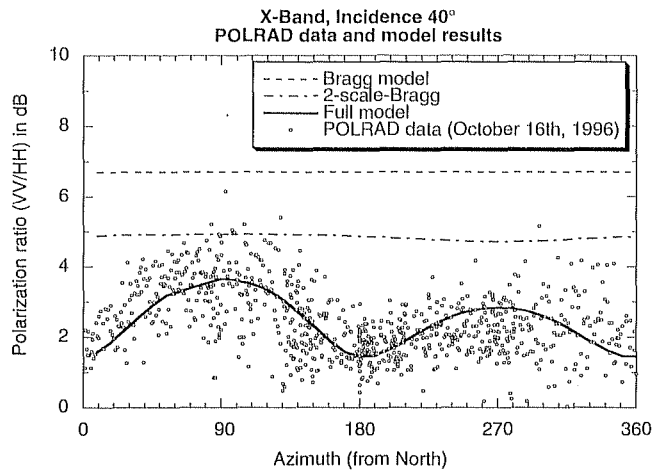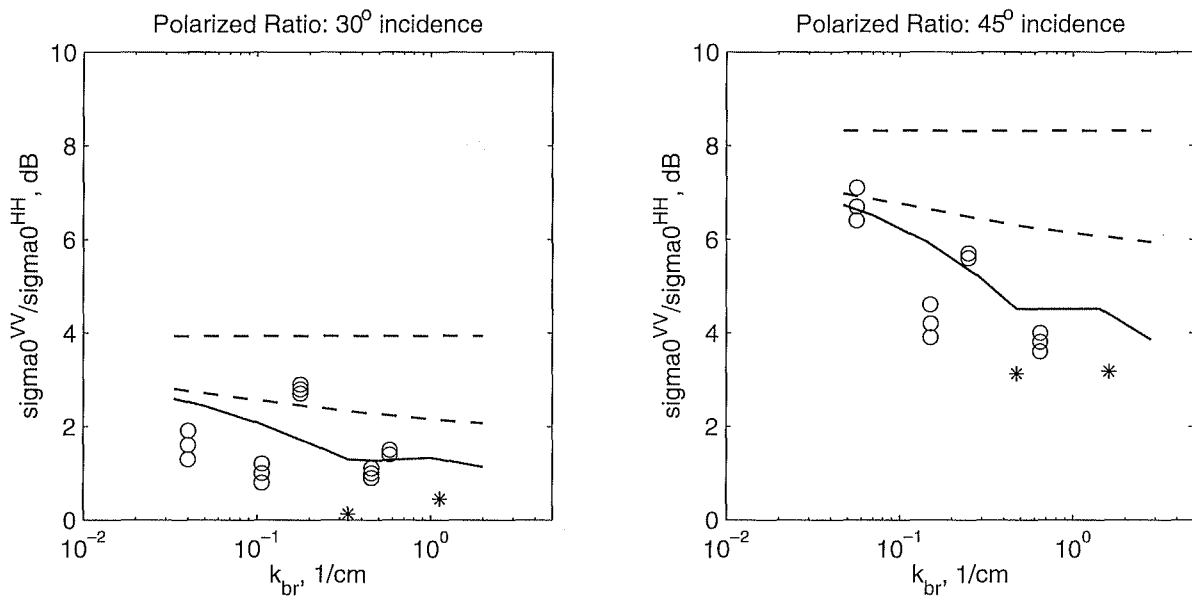
Figure 7. X-band polarization ratio at 40° incidence as a function of radar looking azimuth. Symbols correspond to data obtained during the POLARD-96 experiment (wind speed is about 10 m/s). Dashed line shows the prediction of the pure Bragg model (equation (1)); lower dash-dotted line is the prediction of the composite Bragg model (equation (49)); solid line shows the prediction of the full NRCS model, accounting for the non-Bragg scattering.

POLRAD'96 experiment [*Hauser et al.*, 1997] using the helicopter-borne polarimetric scatterometer "RENE" [*Leloch-Duplex et al.*, 1996]. Figure 7 illustrates the results obtained from one of the three cases collected during this experiment. The two other cases are similar. The observed polarization ratio exhibits a well-pronounced anisotropy in azimuth: the maximal value of P is in the downwind direction, whereas minimum values are in the crosswind

directions. The ratio between upwind and crosswind values of P is about 2dB. *Chapron et al.* [1997] also mentioned a significative difference between HH and VV polarizations for the azimuthal modulation deduced from the NSCAT Ku-band scatterometer observations. The model estimates of the NRCS polarization ratio for the same conditions within the frame of the pure Bragg model (upper dashed line) and composite Bragg model (lower dash-dotted line) are also shown in Figure 7. The first result is that the observed polarized ratio is significantly less than the one predicted by the Bragg theory. The average difference between Bragg theory and observation is about 4 dB for the pure Bragg model and about 2 dB for the composite model. These observations qualitatively imply that there is a mean (azimuthally independent) contribution of non-Bragg scattering mechanism. We associate such a phenomenon with radio waves scattering on breaking waves. The second result qualitatively obtained from this comparison is that the non-Bragg part has also an anisotropic behavior. In our model (see section 4.3) we describe this as an effect of tilting of breakers providing a stronger non-Bragg scattering in the upwind direction (see equation (55)). Figure 7 shows that the introduction in the Bragg model of the cross-correlation of tilt and hydrodynamic modulations does not provide a behavior in azimuth that could explain the observed data.

[44]   Another example of results from the Bragg part of the model is shown in Figure 8, which shows the polarization ratio averaged in azimuth for two incidence angles (Figure 8a at 30°, Figure 8b at 45°) and plotted as a function of the Bragg scattering wave number. Experimental values from *Unal et al.* [1991] and *Masuko et al.* [1986] are also shown in Figure 8. These data relate to wind speeds in the range 8 to 12 m/s. The experimental values of the polarization ratio

Figure 8. Averaged polarization ratio as a function of the Bragg wave number at wind speed 8 to 12 m/s, and at incidence angles 30° (left panel) and 45° (right panel). Dashed lines are predictions of the pure (equation (1)) and composite (equation (49)) Bragg scattering models (upper and lower dashed lines respectively); solid lines are predictions of the full NRCS model (equation (59)), accounting for the non-Bragg scattering. Symbols are radar observations: open circles are from *Unal et al.* [1991]; stars are from *Masuko et al.* [1986].
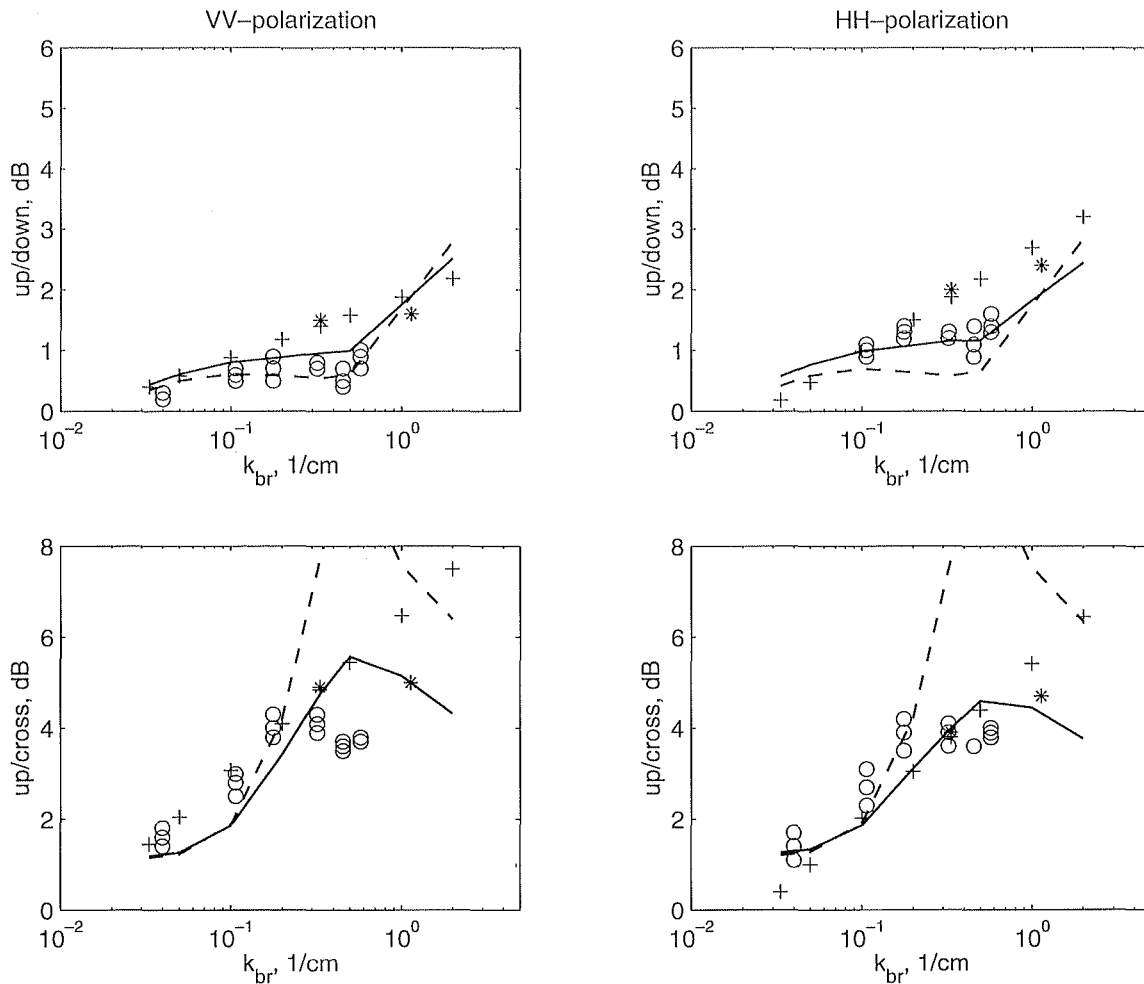
Figure 9. Upwind to downwind ratio (upper panels) and upwind to crosswind ratio (lower panels) as a function of inverse Bragg wavelength, for VV and HH polarization, and at incidence angle 30° and wind speed 8 to 12 m/s. Dashed lines are prediction of the composite Bragg scattering model (equation (49)); solid lines are predictions of the full NRCS model (equation (59)), accounting for the non-Bragg scattering. Symbols are radar observations: open circles are from *Unal et al.* [1991]; crosses are from *Jones and Schroeder* [1978]; stars are from *Masuko et al.* [1986].

increase with increasing incidence angle, and decrease with k_{br}. Results obtained from pure Bragg theory (upper dashed lines), and from two-scale Bragg scattering model (lower dashed line) indicate that the pure Bragg predictions significantly overestimate observations at both incidence angles; the larger is the incidence angle, the stronger is the difference. Accounting for the tilting waves effect (two-scale NRCS model, lower dashed line in Figure 8) results in a decrease of the polarization ratio. Nevertheless, the overestimate of the observed values of P at $\theta = 45°$ remains; at $\theta = 30°$ the overestimate is not so strong, but exists nevertheless. Hence we suggest that the difference between the two-scale NRCS model predictions and the observed values of polarization ratio can be related to the contribution of non-Bragg radar scattering mechanism.

[45] Figures 9 and 10 show observed values of the upwind to downwind ratio of the NRCS for VV polarization (left panels) and HH polarization (right panels) obtained at different Bragg scattering wave numbers from *Unal et al.* [1991], *Jones and Schroeder* [1978], and *Masuko et al.* [1986]. These data relate to wind speeds in the range 8 to 12 m/s, and to

incidence angles of 30° (Figure 9) and 45° (Figure 10). To plot the data of *Jones and Schroeder* [1978] we have used their functional dependence presented in their equation (6), whereas to plot the results of *Masuko et al.* [1986], we have used equation (7) of these authors. Values at 45° have been obtained from an interpolation of their regression coefficients obtained for other incidence angles.

[46] The upwind to downwind ratio of NRCS is larger in HH polarization than in VV polarization. Dashed lines in these plots show the model predictions resulting from the two-scale composite Bragg scattering model. As discussed above, two mechanisms are responsible for the upwind to downwind asymmetry: cross-correlation between hydrodynamic modulations of Bragg waves and slopes of longer tilting waves, tilt of parasitic capillaries. The latter process works if Bragg scattering waves belong to the capillary range. This effect results for the model in a rapid increase of the upwind to downwind ratio in the range of capillary Bragg waves. At VV polarization and at both $\theta = 30°$ and $\theta = 45°$, the Bragg model predictions of the upwind-to-downwind ratio of NRCS, $\sigma_{0up}^{vv}/\sigma_{0down}^{vv}$, are consistent with measurements.
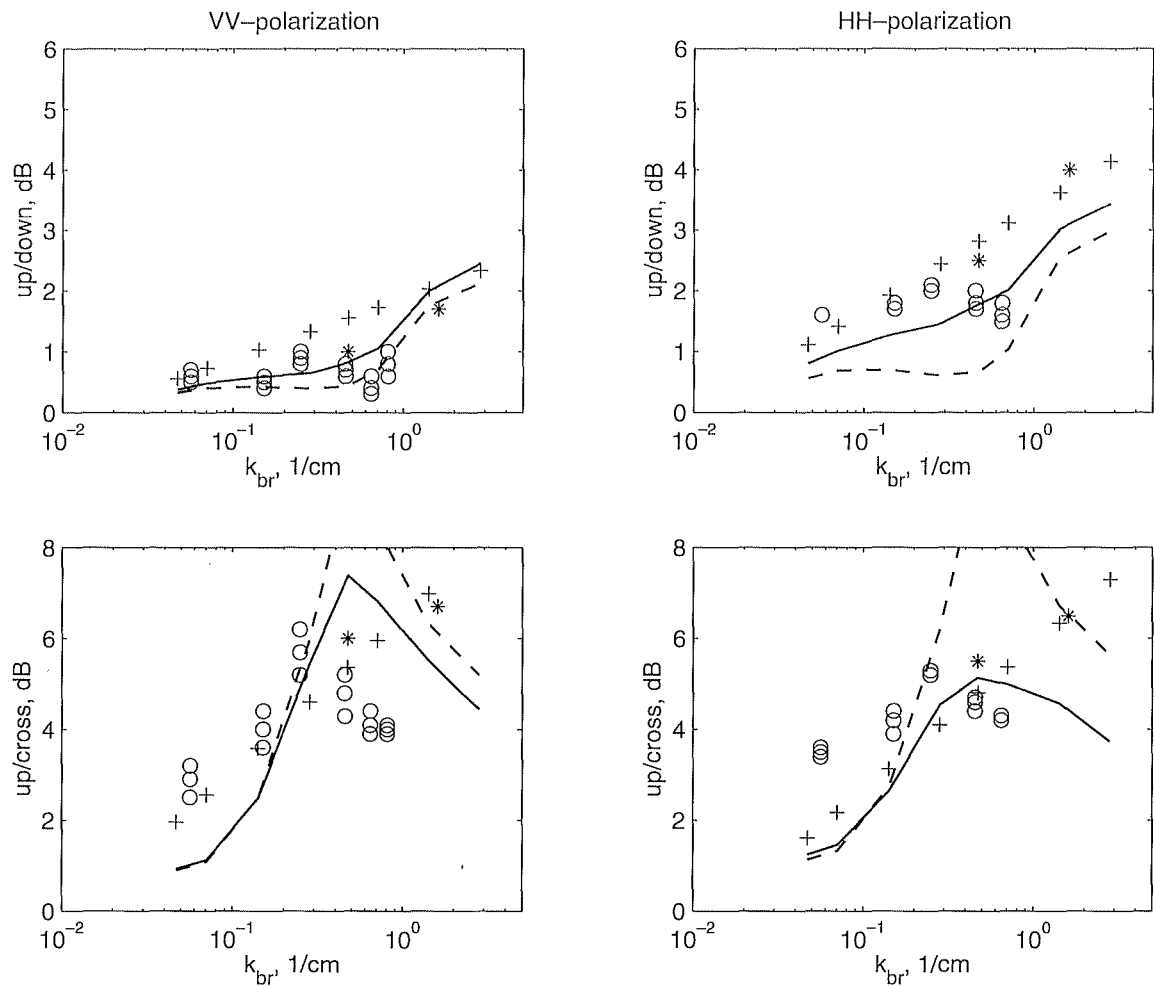
Figure 10.   Same as in Figure 9, but for incidence angle 45°.

For HH polarization and at $k_{br} < 1 \text{cm}^{-1}$, the experimental estimates of $\sigma^{vv}_{0up}/\sigma^{vv}_{0down}$ are larger than the Bragg model predictions. At $\theta = 45°$ this difference is significant (one dB or more). Hence, taking into account hydrodynamic effects in the model is not sufficient to reproduce the observed behavior in azimuth of the radar cross-section.

[47] The bottom plots in Figures 9 and 10 present the experimental and model estimates of the upwind to cross-wind ratio of the NRCS, $\sigma_{0up}/\sigma_{0cr}$. The experimental data illustrate the well-known feature of the radar backscattering from the sea surface: the upwind to crosswind ratio has a well expressed dependence with the Bragg wave number, showing a high degree of anisotropy when k_{br} is in the capillary-gravity range of the spectrum [*Caudal and Hauser*, 1996; *Quilfen et al.*, 1999]. Model estimates of the upwind to cross-wind ratio based on the Bragg scattering model (dashed lines) are consistent in overall with the observations, although there is an apparent overestimation of the model with respect to the observed values at Bragg wave numbers related to X- and Ku-band.

[48] In summary, from the comparison of the Bragg model results with observations of the polarization ratio and of the upwind/downwind ratio in HH, we suggest that an additional non-Bragg scattering process has to be taken into account in the modeling of the total NRCS.

4.3. Non-Bragg Scattering

[49] *Phillips* [1988] originally proposed a phenomenological model for the description of non-Bragg scattering mechanism. This model gives the overall contribution to the NRCS of the scattering areas related to wave breaking events, independent of what concrete mechanism is responsible for the backscattering: specular reflection, wedge scattering or scattering from "rough" structures of broken waves. The general expression relating the contribution of non-Bragg scattering to wave breaking statistics is given by equation (9). Using the relation $\Lambda(\mathbf{k}) \propto u^3 g^{-3/2} k^{1/2}$ for the length of the wave breaking fronts, *Phillips* [1988] obtained:

$$\sigma_{wb}(\varphi, \theta) = C(\varphi, \theta) \left(\frac{u_*^2 k_r}{g} \right)^{3/2} \tag{50}$$

where $C(\varphi, \theta)$ is a function of incidence angle θ and azimuth φ.

[50] Determining this function of two variables from radar observation is quite difficult. To reduce the number of unknown parameters, we use the recent results of *Ericson et al.* [1999] and the conceptual approach of *Wetzel* [1986]. *Ericson et al.* [1999] have investigated the radar scattering mechanisms associated with wave breaking in laboratory conditions. They performed X-band radar measurements at

an incidence angle of 45°, in HH and VV polarizations, and at numerous streamwise positions along stationary breaking waves. They showed that radar returns near the breaking crest are the result of incoherent backscatter due to the generation and tilting of enhanced surface roughness by breaking waves. They observed a polarization ratio of the increased radar returns very close to unity (see their Figure 3). They also showed that the observed radar scattering from the breaking crests was well reproduced by a scattering model in Kirchhoff approximation, while the Bragg theory reproduced radar returns from smoother areas located far from the breaking crests. *Ericson et al.* [1999] concluded that incoherent backscatter from surface disturbances generated by breaking waves may account for the high radar returns (or sea-spikes), and it is not necessary to invoke other mechanisms attributed to extreme shapes of breaking waves to explain the observed behavior of radar scattering from breaking waves.

[51] To model the natural conditions of breaking waves typical of the open ocean, we follow the concept of *Wetzel* [1986, 1990], who propose that breaking is mainly supported by spilling breakers as described by the plume model of *Longuet-Higgins and Turner* [1974]. These spilling breakers are characterized by a plume of rough surface due to breaking elements falling down the wave crest, and having a sharp entry into the underlying long wave [see *Wetzel*, 1990, Figure 32]. Hereafter, we first model the contribution of radar backscatter due to the upper rough surface of the plume. We assume that the radar returns from breaking waves is a sum of individual contributions of increased radar scattering from a discrete set of rough surface areas (the plumes). We further use the statistical description of wave fronts proposed by *Phillips* [1988] to build a model of NRCS, which separates the dependence with incidence and the dependence with azimuth. Then, in section 4.4 we propose a way to take into account the contribution of the sides of the plume which characterize the sharp entry of the plume into the underlying wave.

[52] To simplify the problem, we first consider the case in which the wave field is in a narrow-band surface in the range $\mathbf{k}$ to $\mathbf{k} + d\mathbf{k}$, but with angular energy distribution of arbitrary width. We assume each breaker (or plume) with enhanced roughness to be approximated by a flat surface of area ds_j. The angle between the normal to this area and the vertical direction is θ'_j, and its azimuth (relative to the azimuth φ of the incidence plane) is φ'_j. We assume that the surface roughness of each breaker is isotropic, and that the inverse wave number of breaking waves k^{-1} defines the scale of all statistical characteristics of the roughness, such as its variance, radius of correlation etc. Then the NRCS σ_{0wb} of each of such elements depends on the local incidence angle $\theta_j = \theta + \theta'_j$ (θ is the incidence angle of radar observation), and on the ratio of the radar wave number to the wave number of breaking waves, i.e. $\sigma_{0wb} = \sigma_{0wb}(\theta + \theta'_j, k/k_r)$. Moreover, according to the observations of *Ericson et al.* [1999], we suggest that σ_{0wb} does not depend on polarization. Then, the contribution of non-Bragg scattering to the total NRCS of an observed area S_0:

$$d\sigma_{wb}(\varphi, \theta) = \frac{\sum \sigma_{0wb} ds_j}{S_0} = \sigma_{0wb}(\theta) dq + \frac{\partial \sigma_{0wb}}{\partial \theta} \sum \theta'_j \cos \varphi'_j dq_j$$

$$(51)$$

where $dq = \Sigma ds_j/S_0$ is the fraction of the sea surface covered by the area with increased radar returns, and $dq_j = ds_j/S_0$ is the fraction of individual plumes. The second term in equation (51) describes the tilting effect of enhanced surface roughness due to the fact that the plumes are spread on the forward face of breaking waves. If we assume that the tilt of all scattering areas is approximately the same (i.e. $\theta'_j = \overline{\theta_{wb}}$) then equation (51) takes the form:

$$d\sigma_{wb}(\varphi, \theta) = \sigma_{0wb}(\theta) \left(dq + M_{twb} \overline{\theta_{wb}} \sum \cos \varphi'_j dq_j \right) \qquad (52)$$

where $M_{twb} = (1/\sigma_{0wb}) \partial \sigma_{0wb}/\partial \theta$ is a tilting transfer function, and $\overline{\theta_{wb}}$ is a mean tilt of non-Bragg scattering area.

[53] Following the approach of *Phillips* [1988], we relate the scattering area to the distribution function $\Lambda(k, \varphi)$ of the length of breaking fronts. It is suggested that the contribution of breaking fronts to dq is proportional to $k^{-1} \Lambda(k, \varphi) dk$ [*Phillips*, 1985]; when the angular distribution of breaking fronts is not narrow then $dq \propto dk \int \Lambda(k, \varphi) d\varphi$. Now equation (52) can be rewritten as:

$$d\sigma_{wb}(\varphi, \theta) \propto \sigma_{0wb}(\theta, k/k_r) \Lambda_k(k)$$
$$\cdot \left(1 + M_{twb} \overline{\theta_{wb}} \frac{\int \cos(\varphi - \varphi_1) \Lambda(k, \varphi_1) d\varphi_1}{\Lambda_k(k)} \right) dk \qquad (53)$$

where $\Lambda_k(k) = \int \Lambda(k, \varphi_1) d\varphi_1$ is the distribution of breaking front lengths integrated over all directions. Hereafter we suggest that $\overline{\theta_{wb}}$ does not depend on the wave number of the breaking wave. This is a consequence of the self-similarity of breakers of different scales.

[54] Equation (53) relates to the case of narrow-band wind waves. To obtain a relation valid for the wide wave spectrum, we integrate equation (53) over all breaking waves ($k < k_{nb}$):

$$\sigma_{wb}(\varphi, \theta) \propto \int_{\varphi} \int_{k < k_{nb}} \left(1 + M_{twb} \overline{\theta_{wb}} A_{wb}(\varphi) \right) \sigma_{0wb}(\theta, k/k_r) \Lambda(k, \varphi_1)$$
$$\cdot d\varphi_1 dk \qquad (54)$$

where $A_{wb}(\varphi)$ is the distribution in azimuth of non-Bragg scatters, which is

$$A_{wb}(\varphi) = \Lambda_k^{-1} \int \cos(\varphi_1 - \varphi) \Lambda d\varphi_1$$

[55] Equation (54) is similar to equation (9) originally proposed by *Phillips* [1988]. The advantage of our equation (54) is that it gives the explicit azimuth behavior of σ_{wb} (connected to the angular distribution of wave breaking fronts), and that σ_{0wb} (unlike C in equation (9) has a physical meaning: it is the NRCS of the plume area generated by a breaking wave. According to the results of *Ericson et al.* [1999], the NRCS of breaking waves σ_{0wb} can be computed in the Kirchhoff approximation if the statistical properties of roughness enhanced by breaking waves are known (in particular, roughness elevation covariance; see their equation (8)). However, statistical properties of breaker's roughness are poorly studied and the proportionality coefficient relating dq to $k^{-1} \Lambda(k, \varphi) dk$ is unknown. Thus we have to make some additional assumptions. First of all, it is reasonable to assume that $\sigma_{0wb}(\theta, k/k_r)$ vanishes at large k/k_r, say at $k/k_r > 1$. It means that only breakers with scales exceeding the radar wavelength can contribute to the

increased radar returns (note that the variance of breaker roughness $\tilde{\zeta}_{wb}^2$ is proportional to k^{-2}), hence scattering parameter $k_r^2 \tilde{\zeta}_{wb}^2 \approx (k_r/k)^2$ decreases at large k/k_r. Second, we suggest that a cutoff of σ_{0wb} at large k/k_r can be adopted in the upper limit of integration in equation (54); it means that $k_{nb} = b_r k_r$. Then we have:

$$\sigma_{wb}(\varphi, \theta) = \sigma_{0wb}(\theta) \cdot \left(1 + M_{twb}\overline{\theta_{wb}}A_{wb}(\varphi)\right) \cdot q \qquad (55)$$

where $\sigma_{0wb}(\theta)$ is the NRCS of the plumes, which is now a function of incidence angle only, and q is the fraction of the sea surface covered by these areas generated by wave breaking. Fraction q is described in term of $\Lambda(k, \varphi)$ as:

$$q = c_q \int_\varphi \int_{k<k_{nb}} \Lambda(k, \varphi_1)d\varphi_1 dk \qquad (56)$$

where c_q is a constant.

[56] We have defined the constant b_r as $b_r = 0.1$. This implies that the lengths of waves providing non-Bragg scattering are more than 10 times longer than the radar wavelength. However, we should account for the fact that in case of very short radio waves (e.g. Bragg waves in K-band), the upper limit k_{nb} may relate to too short gravity waves (say, wavelength shorter than 15 cm), which rather generate parasitic capillaries than generate turbulent breakers. We have already suggested that the scattering of radio waves from parasitic capillaries obeys to the Bragg theory, and this fact has already been taken into account in the shape of the spectrum (equation (17) and in the NRCS of the sea surface (see equation (49)) Therefore, the upper limit of gravity waves generating breakers will be further defined as $k_{nb} = \min(b_r k_r, k_{wb})$ with $k_{wb} = 2\pi/0.15$ rad/m. The distribution function $\Lambda(k, \varphi)$ (resulting from the transformation of equation (28) from **c**-space to **k**-space) is:

$$\Lambda(k, \varphi) = \frac{1}{2k}\left(\frac{B(k, \varphi)}{\alpha}\right)^{n+1} \qquad (57)$$

equations (55)–(57) define the contribution of non-Bragg scattering from breaking waves to the NRCS of the sea surface. Constant c_q and function $\sigma_{0wb}(\theta)$ are unknown parameters of the non-Bragg scattering model which have to be adjusted.

[57] To show how this equation relates to Phillips' model (equation (50)), we take into account that the integral in equation (55) converges on the upper limit (which is well inside the gravity range). Then we have:

$$\sigma_{wb}(\varphi, \theta) \propto \sigma_{0wb}(\theta) \cdot \left(1 + M_{twb}\overline{\theta_{wb}}A_{wb}(\varphi)\right) \cdot \left(\frac{u_*}{c_{nb}}\right)^{2+m_g} \qquad (58)$$

where $c_{nb} = (g/k_{nb})^{1/2}$ is the phase velocity at $k = k_{nb}$, and $m_g = 2/n_g$ is the wind exponent in the gravity equilibrium range of the spectrum. Relation (58) can be considered as a generalization of Phillips' model (equation (50)); at $m_g = 1$, and $c_{nb} = b_r^{-1/2}(g/k_r)^{1/2}$, equation (58) coincides with equation (50). The advantage of our model is that it gives the explicit azimuth dependence of non-Bragg scattering, which is directly related to the angular distribution of the breaking fronts.

[58] As M_{twb} is negative, equation (55) indicates that the contribution of non-Bragg scattering to the total NRCS is minimal in the downwind direction and is maximal in the upwind direction of radar observations.

4.4. Parameters of the Non-Bragg Scattering Model

[59] We obtained the explicit relations describing the sea surface NRCS supported by Bragg (equation (49)) and non-Bragg (equation (55)) scattering mechanisms. Statistical properties of the sea surface accounted for in the Bragg scattering model relate to the "regular" surface with spectrum (17) resulting from the energy balance equation. We suggest that such a description of the sea surface is valid outside the breaking zones. Hence, the NRCS due to Bragg scattering has to be restricted by factor $(1 - q)$. The remaining sea surface (with fraction q) provides non-Bragg scattering and statistical properties of these areas (with enhanced roughness generated by wave breaking) differ from the "regular" surface. Hence the full model of NRCS σ_0^p is expressed as the sum of the Bragg component σ_{br}^p and of the non-Bragg component σ_{wb}

$$\sigma_0^p(\theta, \varphi) = \sigma_{0br}^p(\theta, \varphi)(1 - q) + \sigma_{wb}(\theta, \varphi) \qquad (59)$$

where we neglect the contribution of specular reflection from "regular" waves (equation (8)) because we are interested at conditions of moderate incidence angles ($\theta \geq 20°$), where this term has to be small.

[60] For the non-Bragg scattering part σ_{wb} (defined by equation (55)) the function $\sigma_{0wb}(\theta)$ and constant c_q must be specified. These parameters affect the average polarization ratio, while the derivative of $\sigma_{0wb}(\theta)$ versus incidence angle $M_{rwb} = (1/\sigma_{0wb})\partial\sigma_{0wb}/\partial\theta$ times θ_{wb} (averaged tilt of non-Bragg scattering areas) contributes to the upwind-to-downwind ratio. To estimate $\sigma_{0wb}(\theta)$, we use the experimental data reported by *Unal et al.* [1991] and by *Masuko et al.* [1986] shown in Figure 8.

[61] As developed, $\sigma_{0wb}(\theta)$ is the NRCS of the areas covered by plumes (spilling breakers). Following *Ericson et al.* [1999] findings, we suggest that the NRCS of an individual breaking zone can be estimated within the frame of Kirchoff approximation. The NRCS for the quasi-specular reflection described by equation (8) is the known asymptotic solution of the scattering problem in Kirchoff approximation. Since we suggested that only breaking of waves much larger than the radar wavelength contribute to the radar return, then the condition of validity of equation (8) for the case of breakers is fulfilled, and it can be used to parameterize $\sigma_{0wb}(\theta)$. It is clear that an appropriate choice of the mean square slope of the breaker surface (say, it is s_{wb}) allows us immediately to use the shape of equation (8) as a parameterization of $\sigma_{0wb}(\theta)$.

[62] In addition, we have to take into account scattering from the sides of the plume. We follow *Wetzel* [1986, 1990] who assumes a cylindric geometry for this front of the plume, providing specular-condition of reflection whatever the incidence angle is.

[63] To account for this mechanism in our parameterization of $\sigma_{0wb}(\theta)$, we suggest that the local NRCS of the sides of the plume can also be estimated by equation (8) estimated at $\theta = 0°$. We further assume that mean square slope of the breaker sides is the same as the one of its

"cap". Then contribution of the plume sides to the NRCS of the breaking zone can be estimated as $\sigma_{0wb} \propto \varepsilon_{wb} s_{wb}^{-2}$, where ε_{wb} is a constant. Intrinsically the expression for the normalized radar cross-section implies that the constant ε_{wb} represents the ratio of the breaker thickness to its length (because radar cross-sections are normalized by the surface). Since the contributions to the backscatter, of the "cap" of the plume and from its side are independent, the NRCS of the breaking zone reads:

$$\sigma_{0wb}(\theta) = \left(\sec^4 \theta / s_{wb}^2\right) \exp\left(-\tan^2 \theta / s_{wb}^2\right) + \varepsilon_{wb} / s_{wb}^2, \qquad (60)$$

where we recall that s_{wb}^2 is the mean square slope of enhanced roughness (assumed isotropic) of the wave breaking zone. This quantity is wind independent. The second term in (60) becomes dominant at large and grazing incidence angles, in agreement with the well-known fact that at grazing angles, the non-Bragg mechanism is important (see, e.g., *Wetzel* [1990]; or the recent paper of *Churuyomov and Kravstov* [2000]).

[64] To find the constants s_{wb}^2 and ε_{wb} defining σ_{0wb} (θ) (by equation (60)) and constant c_q defining the fraction of the sea surface covered by breaking zones (equation (56)), we use the experimental data reported by *Unal et al.* [1991] and by *Masuko et al.* [1986] and known estimates of the sea surface NRCS at grazing angles. Constants c_q and s_{wb}^2 are chosen so that the model polarization ratio at $\theta = 30°$ and $\theta = 45°$ is in agreement with the experimental observations shown in Figure 8, while constant ε_{wb} is chosen so that the model estimate of $\sigma_0^{hh} \approx \sigma_0^{vv}$ at grazing angles is in agreement with empirical estimates of NRCS at HH polarization (for C-band it is −40 to −30 dB). The set of constants which will be further used in equation (60) is $c_q = 10.5$, $s_{wb}^2 = 0.19$, $\varepsilon_{wb} = 0.005$.

[65] With a proportionality coefficient $c_q = 10.5$, relation (56) gives a reasonable estimate of the fraction of the sea surface covered by breaking zones. It gives $q = 3\%$, at $U_{10} = 10$ m/s, and $q = 18\%$ at $U_{10} = 20$ m/s. Furthermore, with the specified values for s_{wb}^2 and ε_{wb}, the expression for the NRCS of an individual breaking wave gives $\sigma_{0wb} = -3.4$ dB at the incidence angle $\theta = 40°$ and $\sigma_{0wb} = -8.8$ dB at $\theta = 45°$. These estimates are consistent with *Ericson et al.* [1999] measurements. They indeed reported that the NRCS of a breaking wave at $\theta = 45°$ in VV and HH polarization, is −3 dB in the upwave look direction (with a slope of breaking waves of about 5°) and −6 dB in the "downwind" direction.

[66] The last tuning constant to be chosen is the tilt of enhanced scattering areas of breaking waves θ_{wb} (see equation (55)). As it was discussed above, this constant influences the upwind-downwind difference of the NRCS. It is chosen here to match upwind-to-downwind radar observations [*Unal et al.*, 1991; *Jones and Schroeder*, 1978; *Masuko et al.*, 1986] shown in Figures 9 and 10. Accordingly, we fix $\overline{\theta_{wb}} = 5.10^{-2}$. Note that the constant $\overline{\theta_{pc}}$ responsible for the tilt of parasitic capillaries, and used in equations (48)–(49) is also specified as $\overline{\theta_{pc}} = 5.10^{-2}$.

[67] Model predictions of the polarization ratio accounting for the non-Bragg scattering are shown in Figure 8 (solid line). Since σ_{br}^{vv} is larger than σ_{br}^{hh}, the impact of the non-Bragg scattering (which is independent of polarization) results in the decrease of the polarization ratio with respect to the Bragg scattering predictions. An important feature is

that the polarization ratio decreases with increasing radar frequency, in agreement with observations. The predicted upwind-to downwind ratio is shown in Figures 9 and 10 (solid lines, top panels). As expected, the non-Bragg scattering has a larger influence on the upwind to downwind ratio in HH polarization than in VV polarization. Accounting for the non-Bragg scattering also decreases the upwind to crosswind ratio $\sigma_{0up}^p / \sigma_{0cr}^p$ for both HH and VV polarizations.

[68] In summary, accounting for the non-Bragg scattering component is necessary to bring model predictions in closer agreement with observations in terms of polarization ratio, the upwind-to-downwind and upwind-to-crosswind ratios. In the next section, we will further evidence of these features, by comparing the model results with other independent data sets.

5. Results of the Full Model Compared to Observations

[69] Radar observations presented in Figures 8 and 9 were used to adjust the parameters in the non-Bragg scattering part of the NRCS model. Once defined and fixed, we use other radar observations to check the validity of the model.

5.1. Comparison of the X-Band Polarization Ratio From the POLRAD-96 Experiment

[70] Model predictions in the conditions of the POLRAD-96 airborne X-band radar observations are presented in Figure 7. Compared to the case of the Bragg model, accounting for the non-Bragg scattering mechanism significantly improves the agreement between the model predictions and measurements. The non-Bragg scattering inclusion decreases the polarization ratio at all azimuths, and provides a behavior of $P(\varphi)$ with azimuth very similar to the observed one, with maximal values of the polarization ratio in the downwind direction.

### 5.2. Comparison With Empirical Models of ERS and NSCAT at C- and Ku-Bands

[71] Empirical models of the NRCS established for the satellite wind-scatterometers of ERS1-2 (C-band, VV polarization) or for the NSCAT scatterometer (Ku-band, VV and HH polarizations) on the ADEOS platform can also be compared. The wind-scatterometer data from the satellites ERS1-2, and NSCAT are inverted in terms of wind vector by means of empirical models, usually expressed in the form of a truncated series of the look angle (with respect to the wind).

[72] To compare our model results with these empirical models, we express (59) in the form of a truncated Fourier series, which is a standard form of presentation for wind-scatterometer data:

$$\sigma_0^p(\theta, \varphi) = A_0(\theta) - A_1(\theta) \cos(\varphi - \varphi_w) + A_2(\theta) \cos(2(\varphi - \varphi_w)) \qquad (61)$$

where $A_i(\theta)$ are coefficients, which depend on incidence angle, wind speed, and radar frequency. Note that with our convention, the direction $\varphi = \varphi_w$ is the downwind direction, whereas $\varphi = \varphi_w + \pi$ is the upwind direction.

[73] One of the current operational wind retrieval algorithms for the C-band wind-scatterometer of ERS1-2 (in VV
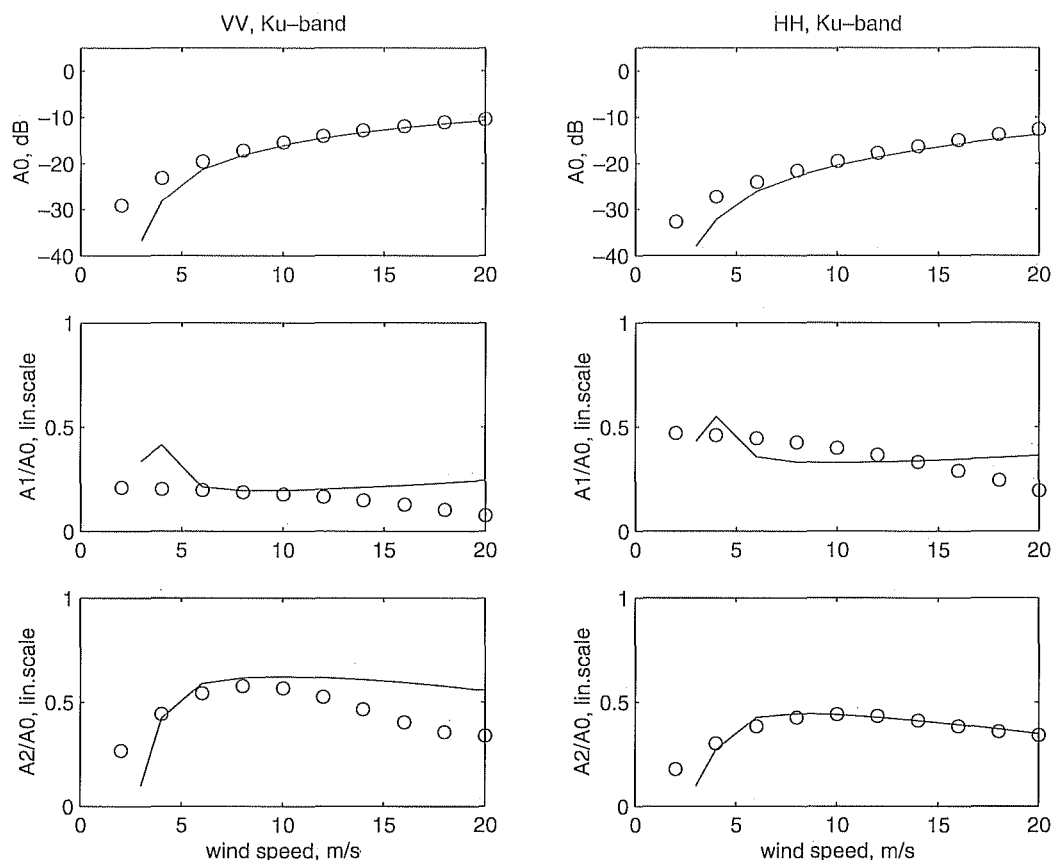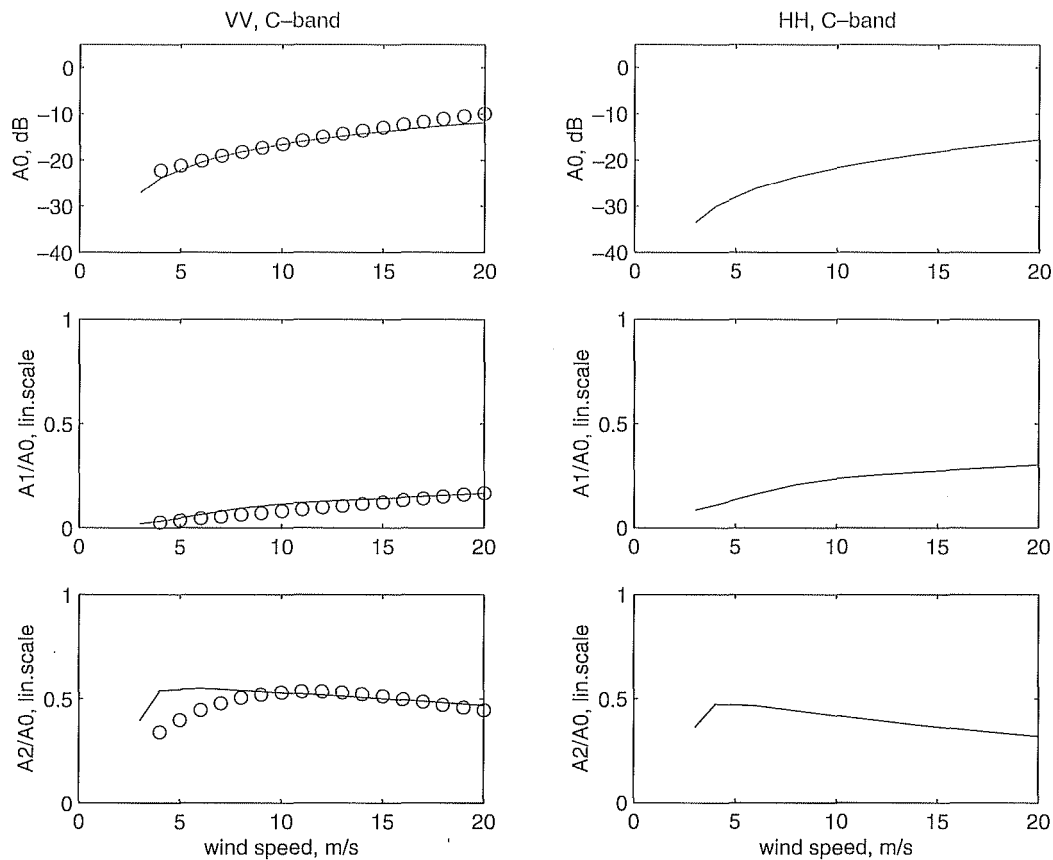
Figure 11. Coefficients of the truncated Fourier series (equation (61)) as a function of wind speed for the Ku-band NRCS, incidence angle 45°, VV polarization (left panels) and HH polarization (right panels). Solid lines are for the present model; open circles refer to the empirical NSCAT model [*Wentz and Smith*, 1999].

polarization) is the so-called CMOD-IFR2 model [*Bentamy et al.*, 1994]. In this model, coefficients of the geophysical function of the type of equation (61) was obtained by collocating triplets of NRCS provided by the wind-scatterometer at three azimuth angles with either wind vector data from meteorological analyses or in situ data. It was independently validated with a large set of in situ data. Similarly, *Wentz and Smith* [1999] proposed an empirical model at Ku-band, VV and HH polarizations derived from the NSCAT observations.

[74] Results of our model in terms of the coefficients A_i^p are compared with the corresponding coefficients of the NSCAT and ERS empirical models in Figures 11 (NSCAT, Ku-band) and 12 (ERS, C-band). These figures show the dependence of the coefficients with wind speed at the incidence angle of 45°. Similar results are obtained at other incidence angles. For ERS, only the VV polarization is available from the observations, whereas for NSCAT, both the VV and HH polarizations are available. The comparison of our model predictions with the empirical functions of NSCAT and ERS, shows that our model reproduces reasonably well all the empirical scattering coefficients A_i^p and their dependence with wind speed. Although we cannot rely on the absolute A_i^p values of NSCAT (NSCAT was calibrated in a relative sense), we can assess the model by the fact that the agreement is quite good for the azimuthally averaged NRCS (coefficients A_0^p) of ERS at moderate and high wind speeds

and for the behavior with wind speed at both polarizations and radar wavelengths. We recall here that the surface model (wave spectrum) was tuned to fit only the observations of an integrated spectral parameter (mean square slope), and that the non-Bragg scattering model was only adjusted to polarization ratio observations. Coefficients A_1^p and A_2^p (normalized by A_0^p) calculated from our model are in reasonably good agreement with the empirical models of ERS and NSCAT. A_1^p/A_0^p is larger in HH than in VV polarization and shows only a weak dependence with wind speed (except at C-band). The empirical values of A_2^p/A_0^p show a local maximum at wind speed around 7 m/s. Our model reproduces a correct behavior of this quantity, with increasing values at light wind and constant or slightly decreasing values at moderate and high winds. The main difference between our results and the empirical values is for A_2^{vv}/A_0^{vv} in Ku-band and VV polarization where we find a nearly constant behavior with wind speed, whereas the empirical results show a decrease of A_2^{vv}/A_0^{vv} with wind speed.

[75] Figure 13 shows the behavior of the azimuthally averaged polarization ratio with wind speed at incidence angles of 30, 45 and 60 degrees. The empirical values (symbols) are here again derived from the geophysical function used for NSCAT. Results of our model are plotted on the same figures for the pure Bragg case (dashed line), composite Bragg (upper solid line) and complete model (composite Bragg plus non-Bragg, lower solid line). At all

Figure 12. Coefficients of the truncated Fourier series (equation (61)) as a function of wind speed for the C-band NRCS, incidence angle 45°, VV polarization (left panels) and HH polarization (right panels). Solid lines refer to the present model, and open circles to the empirical CMOD-IFREMER model [*Bentamy et al.*, 1994].

incidences, the difference between the empirical polarization ratio and the model predictions based on pure Bragg or composite Bragg scattering models is apparent and very strong. None of these models is able to reproduce the order of magnitude of the polarization ratio. This discrepancy increases with incidence angle. In contrast, model calculations accounting for the non-Bragg scattering are quite consistent with the empirical data at all incidence angles: both the order of magnitude and the trend with wind speed

are well reproduced by the model when non-Bragg scattering is accounted for.

5.3. Comparison With Results From RADARSAT at C-Band, HH Polarization

[76] A further assessment of our model is also obtained by comparing the C-band polarization model predictions with available empirical estimates. Figure 14 shows the results of the full model for a wind speed of 10 m/s (solid line). Results
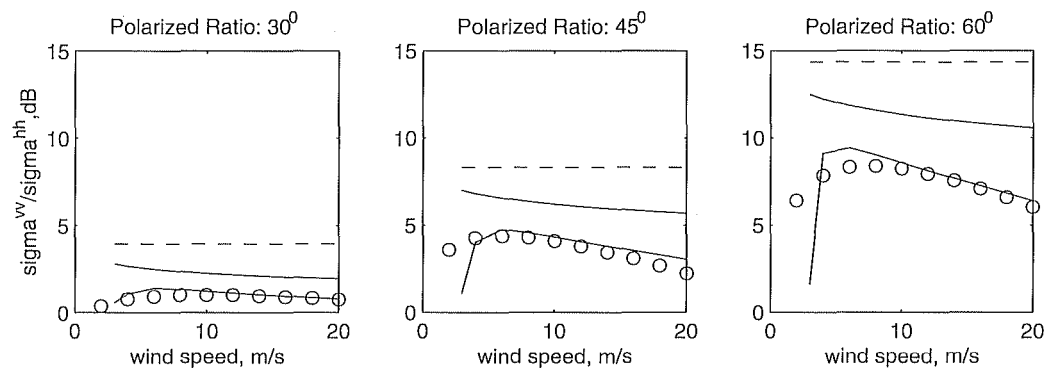
Figure 13. Averaged polarization ratio for Ku-band as a function of wind speed at various incidence angles 30°, 45° and 60°. Open circles are correspond to the empirical NSCAT model; lower solid lines are for the model predictions accounting for the non-Bragg scattering mechanism; upper solid lines are predictions of the composite Bragg model; dashed lines are predictions of the pure Bragg model.

from the pure Bragg model (dotted line) and from the composite Bragg model (dashed line) are also shown in Figure 14. Note that only the composite Bragg model and the full model provide a dependence of the polarization with wind speed (not shown), with a larger dependence with wind speed for the full model. At 40° incidence, the polarization ratio VV/HH for the full model varies from 2.6 to 4.3 dB when wind decreases from 15 to 5 m/s, whereas it varies from 4.7 to 5.3 dB for the composite Bragg model. For comparison, we have plotted in Figure 14, the best fits obtained by *Horstmann et al.* [2000] and by *Vachon et al.* [2000]. *Horstmann et al.* [2000] estimated the polarization ratio at C-band by collocating observations of the RADARSAT Synthetic Aperture Radar (C-band, HH polarization), and data of the ERS-2 scatterometer (C-band, VV polarization). It must be noted that their study shows a large scatter around the best fit (plotted in Figure 14), partly due to the variety of wind conditions and looking angles. *Vachon et al.* [2000] also estimated the polarization ratio in C-band by comparing observed values of NRCS from RADARSAT (HH polarization) with values of NCRS calculated by combining in situ wind measurements and the empirical C-band model valid for the VV polarization. Their results show the polarization ratio to be a function not only of incidence angle, but also of wind speed and look direction with respect to the wind direction. By combining all their estimates, they propose a best fit (plotted in Figure 14). Here again, a large scatter around the best fit is observed in the results of *Vachon et al.* [2000]. For both comparisons, our full model gives polarization ratios which are larger than the experimental best fits, but in better agreement with these empirical results than when a pure Bragg or composite Bragg model is used. Some uncertainties in the data may also come from the fact that the RADARSAT data had to be corrected for a saturation in the received signal [*Vachon et al.*, 2000]. An "hybrid" expression of the polarization ratio was also proposed by *Thompson et al.* [1998] as:

$$\sigma_0^{hh}/\sigma_0^{vv} = \frac{(1 + s\tan^2\theta)^2}{(1 + 2\tan^2\theta)^2} \qquad (62)$$

Based on the study of *Campbell and Vachon* [1997] which also uses RADARSAT data, a value of 0.6 for the parameter s has been proposed by *Thompson et al.* [1998]. Equation (62) with $s = 0.6$ is also plotted in Figure 14. The agreement with our full model is quite good.

5.4. Comparison With Airborne RESSAC Data From the FETCH and SEMAPHORE Experiments

[77] The RESSAC system is an airborne FM/CW radar initially developed for measuring ocean wave directional spectra [*Hauser et al.*, 1992]. It operates at C-band (5.35 GHz) and HH polarization. In its nominal mode it probes the sea surface over the range of incidence angles $7° < \theta < 21°$. During the most recent campaigns (SEMAPHORE in 1993, FETCH in 1998), it was also operated in a mode allowing to measure σ_0^{hh} in the range $27° < \theta < 41°$. By combining these different modes of operation, a method was also developed to deduce the hydrodynamic MTF near 30° incidence angle [*Hauser and Caudal*, 1996].

[78] Figure 15 shows the upwind-to-downwind and upwind-to-crosswind ratio of σ_0^{hh}, obtained by RESSAC

## Polarization ratio at C-Band
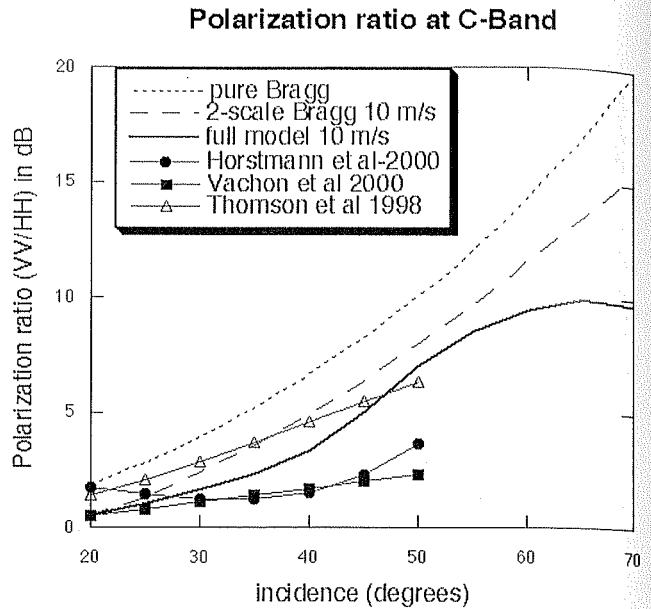
Figure 14. Polarization ratio (VV/HH) in C-band versus incidence angle. Results from the pure Bragg model, composite Bragg and full model (including non-Bragg scattering) at a wind speed of 10 m/s are given by the dotted, dashed and solid lines. Lines with square symbols, and diamonds are the best fit of *Horstmann et al.* [2000], and *Vachon and Dobson* [2000], respectively. Line with triangles is equation (62), with s = 0.6.

during the SEMAPHORE (open square) and FETCH (open circles) campaigns, together with the outputs of our model. The order of magnitude and wind trend of $\sigma_{0up}^{hh}/\sigma_{0down}^{hh}$ (left-hand panel) is satisfactorily reproduced on the average. In the right-hand panel, however, it can be seen that the model cannot reproduce the wind dependence of $\sigma_{0up}^{hh}/\sigma_{0cross}^{hh}$ although it reproduces correctly the average value. Measurements exhibit a clear increase of the upwind to crosswind ratio with wind speed, while the model predicts rather constant behavior with wind speed. To interpret this discrepancy we note that at low winds, the wind direction can be highly variable and this permits to understand why the radar azimuthal signature is much more isotropic than predicted (remind that in the model wind variability is not accounted for). An experimental evidence of the influence of wind variability on the azimuthal anisotropy of the NRCS is given in [*Carswell et al.*, 1999]. At high winds (12–16 m/s), however, the upwind to crosswind ratio measured by RESSAC exhibits large fluctuations (between 3.5 and 6 dB), with average value higher than the model prediction (about 3 dB). The weak dependence of the upwind to crosswind anisotropy of the model with wind speed is explained by the fact that the breaking term does not contribute to the upwind to crosswind difference (it only gives the upwind to downwind wind difference). Hence when the relative role on the non-Bragg scattering increases (with wind speed), it results in a decreasing of the upwind to crosswind anisotropy.

5.5. Summary on the Comparisons

[79] The general conclusion about these comparisons is that the pure Bragg or 2-scale Bragg model overestimates
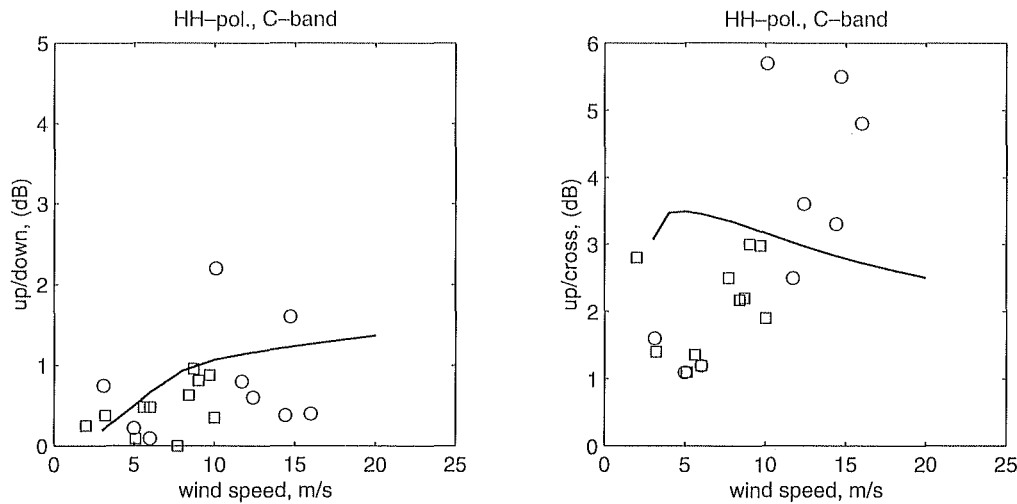
Figure 15. Upwind-to-down-wind ratio (left) and upwind-to-crosswind ratio (right) of the NRCS versus wind speed. Airborne radar observations obtained in FETCH (open circles), and in SEMAPHORE (open squares) experiments. Solid lines are model calculations. Conditions are: C-band, HH polarization, incidence angle 30°.

significantly the polarization ratio. Introducing the non-Bragg scattering gives better agreements with observations. It also explains the large range of variation of the polarization ratio with wind speed mentioned in experimental studies (not shown). Further validation of the model in C-band would require a larger set of observations. In this respect, the launch of ENVISAT, with its multipolarization SAR system will provide a very useful new source of data. In addition, further work is necessary to take into account all the mechanisms (in particular wind variability) which can affect the upwind to crosswind ratio.

6. Conclusion

[80] The general motivation of the study presented in this set of two papers is to build and assess a physical model of the NRCS, which can be applied to various studies related either to the background features of the radar scattering of the sea surface or to the modulations of this backscattering visible in radar images. In this part I we have presented the semiempirical model of the NRCS and assessed it in a large range of radar frequency, incidence angles, and wind conditions.

[81] The NRCS model consists of two modules. The first one describes the statistical properties of the sea surface itself. This description is based on the physical model of short wind wave spectrum (from a few millimeters to a few meters) developed by *Kudryavtsev et al.* [1999], and on the model of statistical characteristics of wave breaking events proposed by *Phillips* [1985]. The combination of these two models gives a description of all the statistical properties of the sea surface (spectrum, mean square slope, wave breaking parameters) that are needed for the electromagnetic part of the model. It is important to note that the surface model has been tuned only to reproduce the observed mean square slope of the sea surface. The second module relates to the calculations of radar backscattering from the surface with known statistical properties. To describe the Bragg scattering component of the sea surface

a standard composite Bragg scattering model is used. The composite model takes into account the influence of long surface waves carrying Bragg scattering waves. This influence is described via tilting and modulation of short waves by longer waves. Both effects can be estimated within the frame of our sea surface model because the wave spectrum is specified in a wide range of wave numbers, and the effect of short wave modulation by longer waves can be easily taken into account. In the capillary range, cross-correlation between modulations of short waves and tilt of longer waves appears, due to parasitic capillaries spread on the forward slope of very short breaking gravity waves.

[82] Comparison of the Bragg scattering model predictions with available radar observations shows that such a model (based on Bragg scattering only) fails to reproduce several characteristics of the data. The main discrepancy relates to the polarization ratio. The Bragg scattering model polarization ratio significantly exceeds the observed polarization ratio at all incidence angles and radar frequencies. In addition, we have shown that even taking into account hydrodynamics effects, the Bragg model is unable to correctly reproduce the upwind to downwind ratio of the NRCS. Hence, both results suggest that some mechanism supporting non-Bragg scattering from the sea surface must be included in the NRCS model.

[83] It has been often suggested that at moderate and large incidence angles, a non-Bragg scattering mechanism connected with breaking waves also contributes to the NRCS. To describe this contribution to the NRCS we used the recent experimental results of *Ericson et al.* [1999]. They showed that incoherent backscatter from surface disturbances produced by breaking waves explains the high radar return, while other possible mechanisms (wedge diffraction, specular reflection etc.) do not necessarily need to be invoked to interpret their data. Using this fact we have modeled the NRCS of the sea surface as a superposition of "regular" sea surface (where backscattering is associated with the Bragg mechanism) and surface

areas with enhanced roughness produced by breaking waves. We have followed the conceptual model of *Wetzel* [1986, 1990], based on the *Longuet-Higgins and Turner* [1974] physical model. Each breaking zone is associated with a spilling breaker characterized by a plume of rough surface falling down the wave crest, and having a sharp entry into the underlying long wave. We have modeled the contribution to radar backscatter due of the upper rough surface of the plume and of its side. To describe the radar response of an ensemble of plume surfaces, the wave breaking statistics proposed by *Phillips* [1985] has been used. The model of non-Bragg scattering is represented by a sum of highly scattering areas (radar targets) with unknown NRCS, which is the main tuning parameter of the non-Bragg scattering model. To estimate this tuning parameter we have suggested that the NRCS of breaking areas can be described as the sum of the NRCS associated with quasi-specular scattering from the upper rough surface of the plumes and of the NRCS associated with the front side of the plumes. Then the determination of the unknown function is reduced to the determination of three unknown constants which are: variance of the slopes of enhanced roughness in the breaking zones (which is wind independent), fraction of the sea surface covered by zones of enhanced roughness (breakers), and ratio of breaker thickness to its length. These constants are defined so that the model azimuthally averaged polarization ratio is in agreement with the observations of *Unal et al.* [1991], and the model NRCS at large incidence angles is in agreement with the one observed at grazing angles. After that the NRCS model is completed.

[84] Validation of the model has been carried out by comparing the model predictions with X-band radar observations of *Hauser et al.* [1997], with the empirical Ku- and C-band NRCS empirical functions for NSCAT and ERS, and with C-band data of the RESSAC airborne data. An overall good agreement in a wide range of incidence angles and wind conditions was obtained. Results show that the polarization ratio is a function not only of radar frequency and incidence angle, but also of wind speed and look direction with respect to the wind direction.

[85] In Part 2, we extend the surface model to analyze the interaction of short waves with longer surface waves and its consequence on the radar Modulation Transfer Function (MTF). We will particularly discuss the results in the HH polarization, because existing models fail to reproduce it. A further validation of the model will be presented by comparing the Hydrodynamic part of the MTF to estimates obtained during the FETCH campaign from the airborne radar RESSAC (C-band, HH polarization).

[86] More generally, because our approach is based on the description of the sea surface which is deduced from the solution of the energy balance equation for the wind generated waves, it gives the possibility to study both the background scattering properties of the sea surface and the response of the radar backscattering to the dynamical processes in the ocean upper layer which affect (via wave-current interaction, for instance) the energy balance in wind generated surface waves. For this goal the energy balance equation of wave in the presence of nonuniform current should be used, with the same energy source/sink terms that was used for the background spectrum.

Appendix A: A Simplification of the Composite Model

[87] Within the frame of the composite model, the NRCS of the sea surface is given by equations (1), (3), (4), and (5). In real condition the mean square slope of the tilting waves is small, therefore these equations can be significantly simplified. We shall evaluate equation (5) to the second order in the slope of the tilting waves. Bragg scattering geometric coefficients $|G_p|^2$ are (remind that x *axis* is directed along the incidence plane)

$$\left|G_v(\theta - \zeta_x, \zeta_y)\right|^2 = |G_v|^2 \qquad (A1)$$

$$\left|G_h(\theta - \zeta_x, \zeta_y)\right|^2 = |G_h|^2 + 2(\zeta_y/\sin\theta)^2 |G_h(\theta)||G_v(\theta)| \qquad (A2)$$

Then the NRCS can be written as

$$\sigma_{br}^v = 16\pi k_r^4 |G_v|^2 k_b^{-4} B_r(\varphi, k_b, \mathbf{x}, t) \qquad (A3)$$

$$\sigma_{br}^h = 16\pi k_r^4 |G_h|^2 k_b^{-4} B_r(\varphi, k_b, \mathbf{x}, t)\left(1 + (\zeta_y/\sin\theta)^2 |G_{v0}|/|G_{h0}|\right) \qquad (A4)$$

where $|G_p| = |G_p(\theta - \zeta_x)|$ and $|G_{p0}| = |G_p(\theta)|$ are geometrical coefficients depending on local and mean incidence angle respectively, $k_b = 2k_r\sin(\theta - \zeta_x)$ is the Bragg scattering wave number at local incidence angle. To the second order in the slope of tilting waves equations (A3)–(A4) can be written as:

$$\sigma_{br}^p = \sigma_{0br}^p\left(1 - M_{t0}^p\zeta_x + \frac{\tilde{B}_r}{B_{r0}} + g^p\zeta_x^2 - \frac{M_{t0}^p}{B_{r0}}\zeta_x\tilde{B}_r\right) \qquad (A5)$$

where $\sigma_{0br}^p = 16\pi k_r^4 |G_{p0}|^2 k_{b0}^{-4} B_{r0}$ is the NRCS of the sea surface without accounting for the tilting effect, $B_{r0} = B_r(\varphi, k_{b0})$ is the background saturation spectrum at $k = k_{b0}$ ($k_{b0} = k_r\sin\theta$ is the Bragg wave number at the mean incidence angle), $M_{t0}^p = (1/\sigma_{0br}^p)\,\partial\sigma_{0br}^p/\partial\theta$ is the so-called tilt component of the radar MTF, $\tilde{B}_r$ is the spectrum variation due to SW modulations by tilting waves, g^p is a polarization coefficient accounting for the impact of the tilting waves in the second order given by:

$$g^v = 1/(2\sigma_{0br}^v)\partial^2\sigma_{0br}^v/\partial\theta^2 \qquad (A6)$$

for the VV polarized scattering, and

$$g^h = 1/(2\sigma_{0br}^h)\partial^2\sigma_{0br}^h/\partial\theta^2 + (2/\sin^2\theta_0)|G_{v0}|/|G_{h0}|\left(\zeta_y^2/\zeta_x^2\right) \qquad (A7)$$

for the HH polarized scattering.

[88] To avoid unnecessary complications, in equation (A5) we have omitted a term describing the change of saturation spectrum in the second order (this term can be defined as a solution of the wave action conservation equation in the second order). From the one hand, this term is negligibly small in comparison with the tilting effect (fourth term in r.h.s of equation (A5); see [*Plant*, 1986]), from the other hand the averaged second order correction of SW spectrum may be simply accounted for in B_{r0}.

[89] Averaging equation (A5) over the scales of the tilting waves (their wave numbers satisfy condition: $k < K_t$ and

assuming that $\overline{\zeta_x} = 0$ and $\overline{\tilde{B}_r} = 0$, we obtain the following relation for the sea surface NRCS:

$$\sigma_{br}^p = \sigma_{0br}^p \left(1 + g^p \overline{\zeta_x^2} - \frac{M_{t0}^p}{B_{r0}} \overline{\zeta_x \tilde{B}_r} \right) \qquad (A8)$$

The second term in the r.h.s of equation (A8) gives the contribution of "pure" tilt effect to the NRCS, while the third term describes the cross-correlation of tilt and hydrodynamic effects. *Plant* [1986] showed that the relative impact of the latter term (in comparison with the "pure" tilt effect) is small. However, within the frame of the composite model only this cross-correlation term is responsible for the NRCS upwind-downwind difference.

References

Banner, M. L., and E. H. Fooks, On the microwave reflectivity of small scale breaking water waves, *Proc. R. Soc. London, Ser. A*, *339*, 93–109, 1985.

Banner, M. L., I. S. F. Jones, and J. C. Trinder, Wavenumber spectra of short gravity waves, *J. Fluid. Mech.*, *65*, 647–656, 1989.

Bass, F. G., I. M. Fuks, A. I. Kalmykov, I. E. Ostrovsky, and A. D. Rosenberg, Very high frequency radiowave scattering by a disturbed sea surface, 2, Scattering from an actual sea surface, *IEEE Trans. Antennas Propag.*, *AP-16*, 560–568, 1968.

Belchor, S. E., and J. C. R. Hunt, Turbulent shear flow over slowly moving waves, *J. Fluid Mech.*, *251*, 109–148, 1993.

Bentamy, A., Y. Quilfen, P. Queffeulou, and A. Cavanié, Calibration and validation of ERS-1 scatterometer, *Tech. Rep. DRO-OS-94-01*, 72 pp., Inst. Fr. Rech. pour l'Exploit. de la Mer (IFREMER), Brest, France, 1994.

Campbell, J. W. M., and P. W. Vachon, Extraction ocean wind vectors from satellite SAR imagery, *Backscatter*, 8(2), 16–21, 1997.

Carswell, J. R., W. D. Donnelly, and R. E. McIntosh, Analysis of C and Ku band backscatter measurements under low-wind conditions, *J. Geophys. Res.*, *104*, 20,687–20,701, 1999.

Caudal, G., and D. Hauser, Directional spreading of the sea wave spectrum at short scale, inferred from multifrequency radar observations, *J. Geophys. Res.*, *101*, 16,601–16,613, 1996.

Chapron, B., V. Kerbaol, and D. Vandemark, A note on relationships between sea surface roughness and microwave polarimetric backscatter measurements: Results from POLRAD-96, in *Proceedings of the International Workshop on POLRAD'96, ESA, WPP-135*, pp. 71–78, Eur. Space Agency, Noordvijk, Netherlands, 1997.

Churuyumov, A. N., and Y. A. Kravstoc, Microwave backscatter from mesoscale breaking waves on the sea surface, *Waves Random Media*, *10*, 1–15, 2000.

Cox, C., and W. Munk, Measurements of the roughness of the sea surface from photograms of the sun's glitter, *J. Opt. Soc. Am.*, *44*(11), 1954.

Donelan, M., J. Hamilton, and W. H. Hui, Directional spectra of wind generated waves, *Philos. Trans. R. Soc. London, Ser. A*, *315*, 509–562, 1985.

Donelan, M. A., and W. J. Pierson, Radar scattering and equilibrium ranges in wind-generated waves with application to scatterometry, *J. Geophys. Res.*, *92*, 4971–5029, 1987.

Duncan, J. H., An experimental investigation of breaking waves produced by towed hydrofoil, *Proc. R. Soc. London, Ser. A*, *377*, 331–348, 1981.

Elfouhaily, T., B. Chapron, K. Katsaros, and D. Vandermark, A unified directional spectrum for long and short wind driven waves, *J. Geophys. Res.*, *102*, 15,781–15,796, 1997.

Ericson, E. A., D. R. Lyzenga, and D. T. Walker, Radar backscattering from stationary breaking waves, *J. Geophys. Res.*, *104*, 29,679–29,695, 1999.

Hara, T., E. J. Bock, and M. Donelan, Frequency-wavenumber spectrum of wind generated gravity-capillary waves, *J. Geophys. Res.*, *102*, 1067–1072, 1997.

Hasselmann, S., and K. Hasselmann, A symmetrical method of computing the non-linear transfer in a gravity-wave spectrum, *Hamb. Geophys. Einzelschr. Ser. A*, *52*, 138 pp., 1981.

Hauser, D., and G. Caudal, Combined analysis of the radar cross-section modulation due to the long ocean waves around 14° and 34° incidence: Implication for the hydrodynamic modulation, *J. Geophys. Res.*, *101*, 25,833–25,846, 1996.

Hauser, D., G. Caudal, G. J. Rijckenberg, D. Vidal-Madjar, G. Laurent, and P. Lancelin, RESSAC: A new airborne FM/CW radar ocean wave spectrometer, *IEEE Trans. Geosci. Remote Sens.*, *30*, 981–995, 1992.

Hauser, D., P. Dubois, and G. Caudal, Polarimetric wind-scatterometer measurements during the POLRAD'96 experiment, *Final Rep. ESA Contract AOP/WK/336073*, Eur. Space Agency, Noordvijk, Netherlands, 1997.

Horstmann, J., W. Koch, S. Lehner, and R. Tonboe, Wind retrieval over the ocean using synthetic aperture radar with C-Band HH polarization, *IEEE Trans. Geosci. Remote Sens.*, *38*, 2122–2131, 2000.

Jähne, B., and K. S. Riemer, Two-dimensional wave number spectra of small-scale water surface waves, *J. Geophys. Res.*, *95*, 11,531–11,546, 1990.

Janssen, P. A. E. M., H. Wallbrink, C. J. Calkoen, D. van Halsema, W. A. Oost, and P. Snoeij, VIERS-1 scatterometer model, *J. Geophys. Res.*, *103*, 7807–7831, 1998.

Jones, L. W., and L. C. Schroeder, Radar backscattering from the ocean: Dependence on surface friction velocity, *Boundary Layer Meteorol.*, *13*, 133–149, 1978.

Kalmykov, A. I., and V. V. Pustovoytenko, On polarization features of radio signals scattered from the sea surface at small grazing angles, *J. Geophys. Res.*, *81*, 1960–1964, 1976.

Kudryavtsev, V., The coupling of wind and internal waves: Modulation and friction mechanism, *J. Fluid Mech.*, *278*, 33–62, 1994.

Kudryavtsev, V., C. Mastenbroek, and V. Makin, Modulation of wind ripples by long surface waves via the air flow: A feedback mechanism, *Boundary Layer Meteorol.*, *83*, 99–116, 1997.

Kudryavtsev, V., V. Makin, and B. Chapron, Coupled sea surface atmosphere model, 2, Spectrum of short wind waves, *J. Geophys. Res.*, *104*, 7625–7639, 1999.

Kwoh, D. S., and B. M. Lake, A deterministic, coherent, and dual-polarized laboratory study of microwave backscattering from water waves, 1, Short gravity waves without wind, *IEEE J. Oceanic Eng.*, *9*, 291–308, 1984.

Leloch-Duplex, N., D. Vidal-Madjar, and J.-P. Hardange, On the calibration of the helicopterborne polarimetric radar RENE, *Ann. Telecommun.*, *51*(5–6), 245–257, 1996.

Longuet-Higgins, M. S., and J. S. Turner, An entraining plume mpdel of a spilling breaker, *J. Fluid Mech.*, *63*, 1–20, 1974.

Lyzenga, D. R., and E. A. Ericson, Numerical calculations of radar scattering from sharply peaked ocean waves, *IEEE Trans. Geosci. Remote Sens.*, *36*, 636–646, 1998.

Mastenbroek, C., Wind-wave interaction, Ph.D. thesis, Tech. Univ. of Delft, The Netherlands, 1996.

Masuko, H., K. Okamoto, M. Shimada, and S. Niwa, Measurements of microwave, backscattering of the ocean surface using X band Ka band Airborne Scatterometers, *J. Geophys. Res.*, *91*, 13,065–13,083, 1986.

Melville, W. K., The role of surface wavebreaking in air–sea interaction, *Annu. Rev. Fluid Mech.*, *28*, 279–321, 1990.

Melville, W. K., M. R. Loewen, F. C. Felizardo, A. T. Jessup, and M. J. Buckingham, Acoustic and microwave signatures of breaking waves, *Nature*, *336*, 54–56, 1988.

Phillips, O. M., *The Dynamics of the Upper Ocean*, 366 pp., Cambridge Univ. Press, New York, 1977.

Phillips, O. M., Spectral and statistical properties of the equilibrium range in the wind-generated gravity waves, *J. Fluid Mech.*, *156*, 505–531, 1985.

Phillips, O. M., Radar returns from the sea surface—Bragg scattering and breaking waves, *J. Phys. Oceanogr.*, *18*, 1063–1074, 1988.

Plant, W. J., A two-scale model of short wind-generated waves and scatterometry, *J. Geophys. Res.*, *91*, 10,735–10,749, 1986.

Plant, W. J., Bragg scattering of electromagnetic waves from the air/sea interface, in *Surface Waves and Fluxes*, vol. 2, *Remote Sensing*, pp. 41–108, Kluwer Acad., Norwell, Mass., 1990.

Plant, W. J., W. C. Keller, V. Hesany, T. Hara, E. Bock, and M. Donelan, Bound waves and Bragg scattering in a wind-wave tank, *J. Geophys. Res.*, *104*, 3243–3263, 1999.

Quilfen, Y., B. Chapron, A. Bentamy, J. Gourrion, T. ElFouhaily, and D. Vandemark, Global ERS 1 and 2 and NSCAT observations: Upwind/crosswind and upwind/downwind measurements, *J. Geophys. Res.*, *104*, 11,459–11,469, 1999.

Romeiser, R., and W. Alpers, An improved composite surface model for the radar backscattering cross section of the ocean surface: Model response to surface roughness variations and the radar imagery of underwater bottom topography, *J. Geophys. Res.*, *102*, 25,251–25,267, 1997.

Romeiser, R., A. Schmidt, and W. Alpers, A three-scale composite surface model for the ocean wave-radar modulation transfer function, *J. Geophys. Res.*, *99*, 9785–9801, 1994.

Schmidt, A., V. Wismann, R. Romeiser, and W. Alpers, Simultaneous measurements of the ocean wave-radar modulation transfer function at L, C, and X bands from the research platform Nordsee, *J. Geophys. Res.*, *100*, 8815–8827, 1995.

Smith, S. D., Coefficients for the sea surface wind stress, heat flux, and wind profiles as a function of wind speed and temperature, *J. Geophys. Res.*, *93*, 15,467–15,472, 1988.

Stewart, R. W., The air–sea momentum exchange, *Boundary Layer Meteorol.*, *6*, 151–167, 1974.

Thompson, D., T. El fouhaily, and B. Chapron, Polarization ratio for microwave backscattering from the ocean surface at low to moderate incidence angles, *Proceedings of IGARSS98* [CD-ROM], IEEE, Piscataway, N.J., 1998.

Toba, Y., Local balance in the air–sea boundary processes, 3, On the spectrum of wind waves, *J. Oceanogr. Soc. Jpn.*, *29*, 209–220, 1973.

Townsend, A. A., Flow in a deep turbulent layer disturbed by water waves, *J. Fluid Mech.*, *98*, 171–191, 1972.

Trokhimoski, Y. G., and V. G. Irisov, The analysis of wind exponents retrieved from microwaves radar and radiometric measurements, *IEEE Trans. Geosci. Remote Sens.*, *18*, 470–479, 2000.

Tran, V. B. N., Contribution a l'etude des diffusometres NSCAT et ERS2 par modelisation neuronale, Influence de la hauteur des vagues sur le signal diffusiometrique, These de doctorat, Univ. Paris VI, Paris, 1999.

Unal, C. M. H., P. Snoeij, and P. J. F. Swart, The polarization-dependent relation between radar backscatter from the ocean surface and surface vector at frequencies between 1 and 18 GHz, *IEEE Trans. Geosci. Remote Sens.*, *29*, 621–626, 1991.

Vachon, P. W., and F. W. Dobson, Wind retrieval from RADARSAT SAR images: Selection of a suitable C-Band HH polarization wind retrieval model, *Can. J. Remote Sens.*, *26*(4), 306–313, 2000.

Valenzuela, G. R., Theories for the interaction of electromagnetic and ocean waves—A review, *Boundary Layer Meteorol.*, *13*, 61–85, 1978.

Wentz, F. J., and D. K. Smith, A model function for the ocean-normalized radar cross-section at 14 GHz derived from NSCAT observations, *J. Geophys. Res.*, *104*, 11,499–11,514, 1999.

Wetzel, L. B., On microwave scattering by breaking waves, in *Wabe Dynamics and Radio Probing of the Ocean Surface*, edited by O. M. Phillips and K. Hasselmann, pp. 273–284, Plenum, New York, 1986.

Wetzel, L. B., Electromagnetic scattering from the sea at low grazing angles, in *Surface Waves and Fluxes*, vol. 2, *Remote Sensing*, pp. 109–171, 1990.

Winebrenner, D. P., and K. Hasselmann, Specular point scattering contribution to the mean synthetic aperture radar image of the ocean surface, *J. Geophys. Res.*, *93*, 9281–9294, 1988.

Wright, J. W., A new model for sea clutter, *IEEE Trans. Antennas Propag.*, *AP-16*, 217–223, 1968.

Zhang, X., Capillary-gravity and capillary waves generated in a wind wave tank: Observation and theories, *J. Fluid Mech.*, *289*, 51–82, 1995.

G. Caudal and D. Hauser, Centre d'Etude des Environnements Terrestres et Planétaires, Centre National de la Recerche Scientifique, Université de Versailles, Vélizy, France. (hauser@cetp.ipsl.fr)

B. Chapron, Institut Français de Recherche pour l'Exploitation de la Mer, Plouzané, France.

V. Kudryavtsev, Marine Hydrophysical Institute, National Academy of Science, Sebastopol, Ukraine.